ABSTRACT

TITANIUM NITRIDE AS AN ELECTRODE MATERIAL FOR HIGH CHARGE DENSITY APPLICATIONS

by
Mustafa Khan Patan

Present day neural prostheses require electrodes with high current densities. Traditional electrodes are not capable of delivering such high current densities. Titanium nitride as an electrode material and other techniques like reactive ion etching, platinization of titanium were studied in this thesis towards improving charge density of electrodes.

Titanium nitride (TiN) was sputtered in a custom designed pattern of electrodes with silicon as substrate, at a deposition rate of 2 A^0/sec. Atomic Force Microscopy (AFM) analysis of TiN film showed a smooth surface for a film thickness of 1μm. X-Ray Diffraction (XRD) analysis of the film showed the presence of TiN and Ti on the substrate.

Reactive Ion Etching (RIE) of the electrode surface with CF_4 and SF_6 for different combination of chamber parameters gave a peak CIC of 65.2 $\mu C/cm^2$. Platinization of Ti in chloroplatinic acid (H_2PtCl_6) provided a maximum Charge Injection Capacity (CIC) of 2.6mC/cm^2.

Electrodes made at University of Michigan were used as reference for all measurements conducted on NJIT patterned electrodes. Other methods to investigate CIC dependencies showed that CIC is not scalable with size, although CIC is calculated per unit surface area. Large surface area electrodes (4000μm^2) had higher CIC per unit surface area and it decreased for smaller electrodes (1250μm^2 and 177μm^2). Electrodes

tested within the water window of hydrolysis showed CIC was dependent on bias voltage and pulse width.

An extended voltage limit in the cathodic cycle increased CIC of TiN coated electrodes significantly. The maximum injectable charge was 4.45mC/cm^2 for a bias voltage of -0.8V.

It can be concluded that electrodes with rough surface had higher charge injection capacity and the charge injection capacity dependencies show that simple elements are not enough for modeling the electrode-electrolyte interface.

TITANIUM NITRIDE AS AN ELECTRODE MATERIAL FOR HIGH CHARGE DENSITY APPLICATIONS

by
Mustafa Khan Patan

A Thesis
Submitted to the Faculty of
New Jersey Institute of Technology
in Partial Fulfillment of the Requirements for the Degree of
Master of Science in Electrical Engineering

Department of Electrical and Computer Engineering

May 2007

APPROVAL PAGE

TITANIUM NITRIDE AS AN ELECTRODE MATERIAL FOR HIGH CHARGE DENSITY APPLICATIONS

Dr. Mesut Sahin, Thesis Co-Advisor — Date
Assistant Professor of Biomedical Engineering, NJIT

Dr. Durgamadhab Misra, Thesis Co-Advisor — Date
Professor of Electrical and Computer Engineering, NJIT

Dr. Dentcho Ivanov, Committee Member — Date
Director, Microelectronics Fabrication Center and Research Professor
Biomedical Engineering, NJIT

BIOGRAPHICAL SKETCH

Author: Mustafa Khan Patan

Degree: Master of Science

Date: May 2007

Undergraduate and Graduate Education:

- Master of Science in Electrical Engineering,
  New Jersey Institute of Technology, Newark, NJ, 2007

- Bachelor of Science in Instrumentation Engineering,
  Osmania University, Hyderabad, A.P, India, 2005

Major: Electrical Engineering

بسم الله الرحمن الرحيم

"In the name of Allah, Most Gracious, Most Merciful"

To my parents, to my sisters Asifa, Shaza and to my brother Sarfaz

ACKNOWLEDGMENT

I would like to thank Dr. Mesut Sahin for being my co-advisor, for his continuous help, for giving me the opportunity to learn valuable techniques like X-Ray Diffraction, Atomic Force Microscopy and for giving me the chance to work in the clean room. I am sure the techniques learned during my thesis will be an asset for my career. I would also like to thank Dr. Durgamadhab Misra who not only served as my co-advisor but also provided help in designing mask for fabrication of electrodes. I would also like to thank Dr. Dentcho Ivanov for being my committee member and for his valuable lectures on safety and principles of fabrication.

Fellow students Ammar Abdo, Abhishek Prasad and Tosha Sha also deserve appreciation for their support and encouragement.

I would like to extend my special thanks to Dr. Rajendra Jerwal and Mr. Lev Markov from Microfabrication Center NJIT and Mr. Chandrakanth Patel from Material Characterization Laboratory.

TABLE OF CONTENTS

TABLE OF CONTENTS
(Continued)

Chapter **Page**

LIST OF TABLES

LIST OF FIGURES

LIST OF FIGURES
(Continued)

LIST OF FIGURES
(Continued)

Figure **Page**

CHAPTER 1

INTRODUCTION

An action potential (Figure 1.1) is a wave of electrical discharge that is generated in the soma and travels along the axon of a neuron. Each cell contains ions distributed inside and outside the cell, the distribution of ions across the cell membrane and the permeability of the membrane to these ions generate a voltage (potential difference). The voltage is negative inside the cell with respect to outside. Resting potential is the potential difference between inside and outside the cell at rest and approximately equals to -70 mV [1].

An action potential is generated when an excitatory stimulus causes a local membrane depolarization, in which at somevoltage; gated sodium channels of the nerve cell membrane open and sodium ions diffuse inside the cell. The sodium ions continue moving inside until the action potential reaches a peak which is approximately around +30 mV [2]. Positive sign means inside of the cell membrane is positive with respect to outside.

After reaching the peak the sodium channels will close and the potassium channels will open. The potassium ions will start diffusing outside the cell. As a result, the re-polarization of the cell membrane would occur and inside will be negative with respect to outside. In this way, the action potential is generated in the soma and would continue to propagate along the axon.

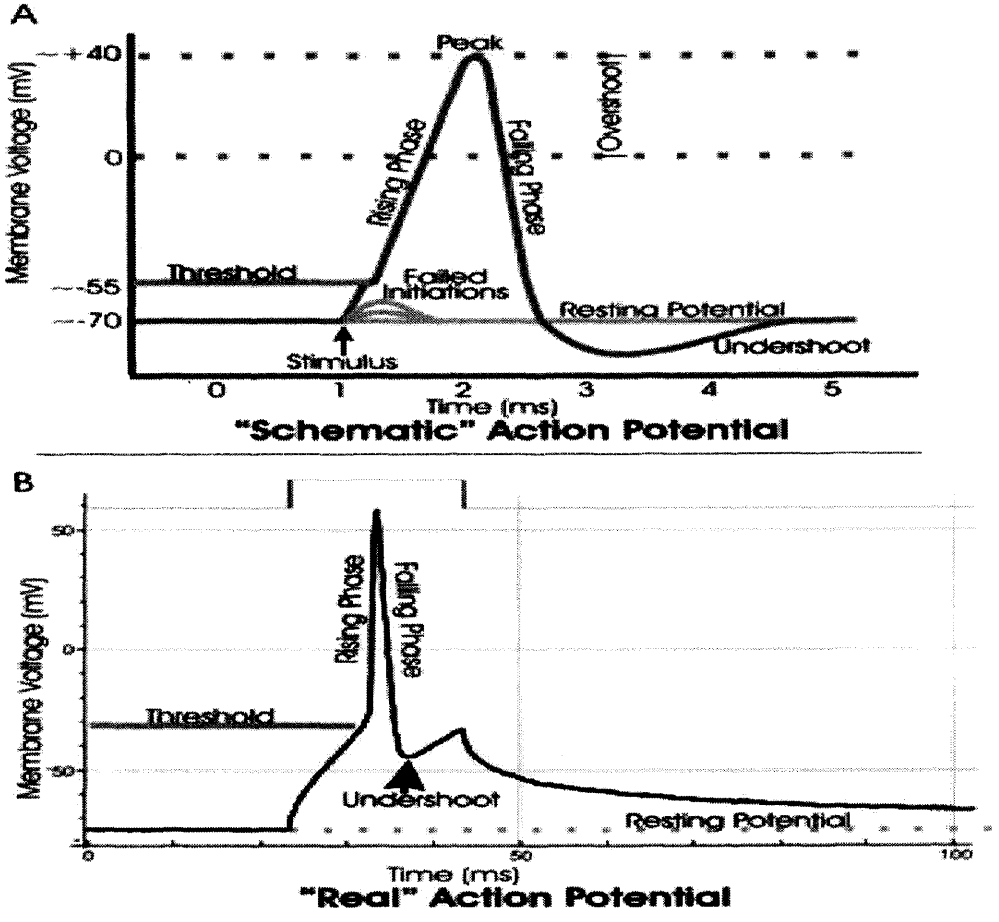

Figure 1.1 Simulated action potential (A) and real action potential (B) generated in the soma [3].

Biopotential electrodes have been widely used for recording currents in the body, and as stimulating electrodes as well. An interface is necessary in order to measure biopotentials from the body. Biopotential electrodes functioning as transducers serve as this interface.

In order to sense electrical signals from the body there must be an exchange of current across the interface. When measuring the resistance of a metal using a voltmeter, the complexity of interface between voltmeter probe metal and the measuring metal is not of concern as the exchange of current across these two metals is due to the movement of

electrons in both entities. This is not the case when measuring the resistance of a solution (electrolyte), because the flow of current in metal is due to electrons and in electrolyte it is due to ions. Hence the phenomena occurring at the electrode-electrolyte interface is of concern.

The electrode-electrolyte interface is schematically illustrated in Figure 1.2. The total current that crosses the interface, passing from the electrode to the electrolyte, consists of electrons-moving in a direction opposite to that of the current in the electrode, cations in the same direction as the current and anions moving in a direction opposite to that of the current in the electrolyte. For the charge to cross the interface there are no free electrons in the electrolyte and there are no cations or anions in the electrode. Some thing must occur between the interfaces that transfers the charge between the carriers. What actually occur are chemical reactions at the interface. These chemical reactions can be represented in general by the following equations: [4]

$$C \Leftrightarrow C^{n+} + ne^- \tag{1.1}$$

$$A^{m-} \Leftrightarrow A + m\,e^- \tag{1.2}$$

Figure 1.2 Schematic of electrode-electrolyte interface.

Here n and m are valence of C and A respectively. The reaction involving cations is shown by the equation 1.1. Here the metal of the electrode at the interface can oxidize to form cation and one or more free electrons, the cation is discharged into the electrolyte and the electrons remains as charge carriers in the electrode. Similarly the reaction involving anion is shown by the equation 1.2. In this case an anion coming to the electrode-electrolyte interface can be oxidized to a neutral atom, giving off one or more free electrons to the electrode.

An important note here is, these reactions are completely reversible, meaning reduction reaction moving from right to left can occur as well. The direction of reaction is determined by the direction of flow of current in the Figure 1.2, if the current direction is to right then oxidation reactions dominates if the current direction is opposite, reduction reactions dominates. These reactions attain equilibrium with rate of oxidation equal to rate of reduction when there is no current.

The equilibrium attained when there is no current flowing is a dynamic equilibrium. When a metal is placed into a solution containing ions of that metal, reaction in eqaution 1.1 starts immediately, initially, the reaction goes predominantly either to left or to right, depending on the concentration of cations in the solution and the equilibrium condition for that particular reaction. As result the concentration of cations and the concentration of anions get affected. The overall result is the neutrality of charge is not maintained around this region. Thus the electrolyte surrounding the metal is at different potential from rest of the solution. This difference in potential is known as half cell potential.

This half cell potential in the immediate vicinity of electrode is determined by metal involved the concentration of ions in the solution and temperature. It is not possible to measure half cell potential with out a reference electrode, as the secondary electrode also has half cell potential. What we finally end up measuring is the difference of potential between these two electrodes. To standardize these measurements, the half cell potential of the standard hydrogen electrode is arbitrarily set to zero. Half cell potential of other electrodes is expressed as a potential difference with this standard electrode.

The half cell potentials of many metals used for electrodes are known and measured with respect to the hydrogen electrode under STP (Standard Temperature (270^{o}c) and Pressure (1 atmosphere)) conditions. When measurements are made in the lab atmosphere, STP conditions are not maintained, as a result half cell potential is altered from that of standered measurements. As the electrode comes in contact with the solution concentration- the activity would change (availability of an ionic species in solution to enter into a reaction). These variations in the half cell potential is modeled by Nernst and is as shown.

$$E = E_o + \frac{RT}{nF} ln\,(acn^{+}) \qquad (1.3)$$

where

E : half-cell potential

Eo : standard half-cell potential

n : valence of electrode material

acn+ : activity of Cation Cn^{+}

T : temperature in Kelvin and

F : faraday's constant.

Studies should that, as the current flows between the electrode and electrolyte, the measured half cell potential is often altered from conditions in which there is no current flow. This variation in half cell potential is due to polarization of the electrode and is termed as overpotential. Overpotential is a sum of three basic components: the ohmic overpotential (V_r), the concentration overpotential (V_c) and the activation over potential (V_a).

The ohmic overpotential is as a result of resistance offered by the electrolyte, when current flows between the two electrodes immersed in the electrolyte. This drop is proportional to current and the resistivity of the electrolyte; follows not necessarily Ohm's law as it is dependent on the concentration of the ions in the solution.

The concentration overpotential results from the change in the distribution of ions at the electrode-electrolyte interface. When a metal is introduced into the solution containing its ions, the reactions in equation 1.1 and 1.2 start instantanously and will reach equilibrium as there is no current flowing across the interface. The equilibrium is not attained if there is current across the interface assisting a direction of reaction. Thus an expected change in the concentration of ions is observed. This change results in a different half cell potential at the electrode. The difference between this and the equilibrium half cell potential is termed as concentration overpotential.

In order that a metal atom gets oxidized to a metal ion and move into the solution, the atom most over come a energy barrier, similarly in the reverse reaction; in which the a cation is reduced and is depositing as metal on the electrode also involves an

activation energy. These two energies are not necessarily same. When there is current between the electrode and electrolyte, the direction of current assists either oxidation or reduction and hence the height of the energy barrier is determined by the direction of current. This difference in energy appears as a difference in voltage across the interface and is know as activation overpotential.

Depending on what happens to an electrode when current passes between it and the electrolyte, there are two types of electrodes- *Perfectly non-polarizable* electrodes are those electrodes in which current passes freely across the interface, requiring no energy to make the transition. *Perfectly polarizable* electrodes are those in which no actual charge crosses the electrode-electrolyte interface when a current is applied. In these electrodes the current across the electrodes is displacement current, and the electrode behaves as a capacitor.

Neither of these two electrodes is possible to make- but some electrodes come close to perfectness. Electrodes made of silver/silver chloride behave close to non-polarized electrodes and electrodes made from noble metals behave close to polarized electrodes.

The electrode-electrolyte interface must be able to transfer electrical stimulation and sense neural response. This requires the material to interact electrochemically with the surrounding tissue in a predicted and controlled manner to ensure adequate operation in the body. This can only be achieved by proper modeling of this interface; modeling also helps in improving repeatability. Primary understanding of this interface as a capacitor was proposed by Helmholtz. Electronic circuit pioneer Varley [5] in 1871 measured this interface capacitance using 1-inch square platinum electrode in contact

with sulphuric acid and reported its value as 311μF . Later in the year 1879 Helmholtz made attempts to model this interface, according to him a double layer of charge exits at the interface as shown in the Figure 1.3. Moreover, because the voltaic cell delivers direct current which has to pass through interface, resistance must also be a component of any model.

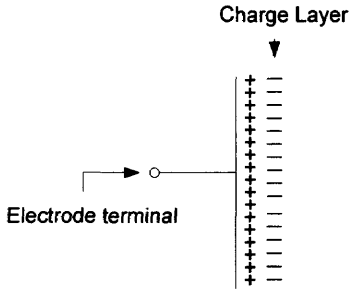

(a) Helmholtz 1879 [6]

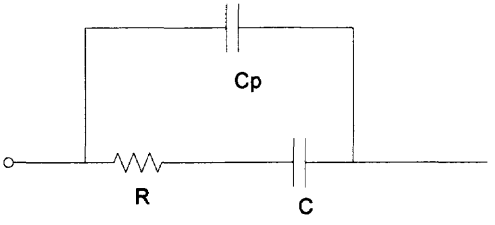

(b) Randles 1947 [7]

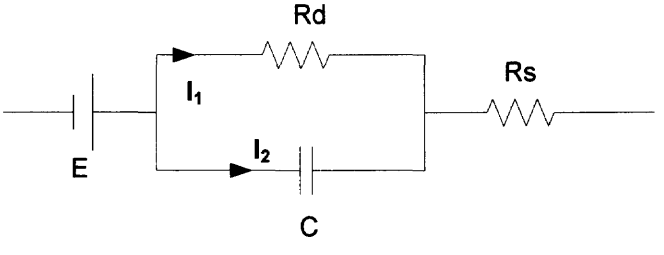

(c) Resent

Figure 1.3 Electrode-electrolyte interface models.

Randles based on his experiments with dropping mercury electrode synthesized a circuit model consisting of Helmholtz double layer (C), polarization capacitance (C_p) and a series resistance (R) as shown in Figure 1.3 (b).

Recently a model explaining the variation of electrode-electrolyte impedance with frequency as shown in Figure 1.3 (c) was proposed. In this model, when the frequency is

very low, the capacitor (C) effectively blocks current I_2 and the resulting impedance is due to current I_1 flowing through R_d and R_s, hence the total impedance is R_d+R_s which is very high. However if the frequency is high, capacitor (C) is effectively short circuited and only current I_2 will flow through R_s resulting in a impedance of only R_s which is acceptable. These models are in evolution adapting to explain various phenomena occurring at the interface.

As the ambitions of scientist grow to enhance the spacitial resolution of specific neural stimulation or sensing devices, the need for micro electrodes with high charge transfer capabilities are of critical importance. The sizes of these micro electrodes are shrinking to accommodate more of them in a given area, especially for vision prosthesis. On the other hand, the electrical limits for these electrodes are below empirically established neural damage limits ($400\mu C/ cm^2$ versus $1mC/cm^2$) [8, 9, 10], thus posing a challenge to fabricate electrodes with high effective surface area and consequently with high charge injection capacities. This can only be achieved by investigating composite materials with micro porous structures in regular fashion like titanium nitride (TiN) [11].

When choosing material for micro electrodes, material properties, surface structure and charge transfer characteristics have to be considered. The charge transfer should take place by double-layer charging/discharging and reversible faradic reactions, as the reversibility of the reaction on an electrode is essential for both biocompatibility and life time of the electrode. Reversibility prevents degradation of electrode and formation of by-products that can harm the body [12]. The surface of the electrode is important for electrode stimulation since it affects the growth of electrode into the tissue and also influences parameters like charge injection capability, electrode impedance and

electrode polarization. Biocompatibility of an electrode is also an important issue as, it is expected to be non-toxic and the threshold values of stimulation should not increase with the growth of fibrous tissue around it [13].

Rough electrode surface structures (TiN columnar structure) have been reported to exhibit high effective surface area, i.e. low impedance and high charge capacity [14,15]. As TiN electrodes have excellent mechanical stability, it is obvious to expect electrodes made of TiN to behave as electrode made of noble metals (close to polarizable electrodes). In polarizable electrodes the charge transfer across the electrode-electrolyte is mainly due to capacitive mechanism. TiN uses capacitive charging of the electrode surface to effectively cause current to flow in the tissue by charge redistribution. The electrode/electrolyte interface impedance can be modeled as a capacitive element.

As shown in Figure 1.4 if we model the electrode-electrolyte interface with R_d and C as resistor and capacitor of the interface respectively, R_s as resistance of the electrolyte. Capacitance is due to presence of double layer of charge on the surface of electrode. As discussed previously, when frequency is very low, the total impedance is R_s+R_d which is high. However if the frequency is high the impedance is only R_s, which is acceptable. This clearly indicates the impedance of the electrode-electrolyte interface is frequency dependent. Another way to alter this impedance is, by fabricating electrodes with high effective surface areas.

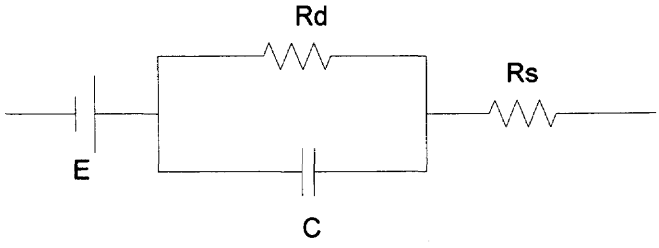

Figure 1.4 Electrical model for electrode-electrolyte interface.

$$R = \frac{\rho l}{A} \tag{1.4}$$

$$C = \epsilon_0 \frac{A}{d} \tag{1.5}$$

where

ρ : resistivity

l: length

A: surface area

ϵ_0 : permittivity of free space

d: distance of separation

The fact that resistance is inversely proportional to surface area (1.4) and capacitance is directly proportional to surface area (1.5) can be explored to achieve higher charge delivering electrodes, even as the size of electrodes shrink's to micro scales.

Since body is tolerant to TiN coating [16] and because of its excellent Mechanical and Chemical stability it is being used in numerous medical (Pace maker electrodes [17], implants, surgical tools etc) applications. Additionally it has an advantage that it is commonly used in the integrated circuit fabrication process, so devices that are fabricated in this fashion will not require special methods for material deposition. Studies showed

that TiN coatings synthesized using vacuum based techniques like magnetron sputtering, ion-plasma, cathodic vacuum arc etc, at relatively high pressures and low substrate temperatures [18], usually have nano or sub-micro crystalline structures [19] and as result have enhanced physical and mechanical properties [20]. Table 1.1 and Figure 1.5 shows formation of grains of different sizes on samples prepared by different vacuum based techniques.

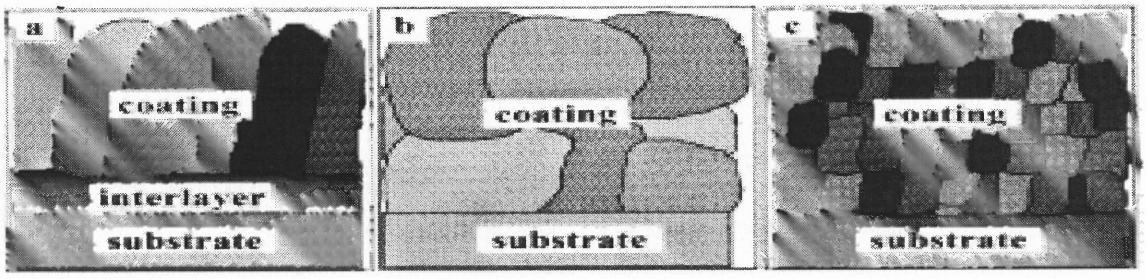

Figure 1.5 Schematic images of the coating grain microstructures: (a) PVD, (b) CVD and (c) PMD.

Table 1.1 Grain Size of Samples Prepared by Different Techniques

TiN coating	Mean grain size
1.PVD – Low voltage high current	0.1μm
2.PVD cathodic arc	0.2μm
3.CVD Surface zone	0.6μm
4.CVD ~ 1μm below Surface	0.4μm
5.PMD	0.06μm

Not until recently, owing to its remarkable properties and growing applications in the field of medicine efforts were made to understand the physical properties of titanium nitride. Table 1.2 lists the physical properties of TiN coating on a substrate using physical vapor deposition.

Table 1.2 Physical Properties of Titanium Nitride (TiN) Coating [21]

Composition	TiN. >99% purity.
Process	PVD Vacuum Deposited Coating.
Appearance	Metallic Gold.
Thickness	Ranges from 0.25 to 12 microns. Typical applications are 1 to 5 microns.
Uniformity	Coating conforms uniformly to the substrate.
Hardness	Hardness > 2000 kg/mm^2 Knoop or Vickers Micro hardness.
Toxicity	Non-toxic. Meets FDA guidelines and has been approved for use in numerous medical/surgical devices, including implants. Meets requirements of FDA and USDA for food contact.
Temperature Resistance	Begins to oxidize at 600° C. (1100° F.) in air. More resistant in an inert atmosphere.
Melting Point	2930° C.
Deposition Temperature	Ranges from 200 to 450° C.
Electrical Resistivity	25 μOhm-cm.
Chemical Resistance	Highly inert to acids, bases, solvents, caustic, etc.
Thermal Expansion Coefficient	9.4 x 10^{-6} /°C.
Thermal Conductivity	0.046 Cal/sec-cm-°C.
Density	5.22 g/cm^3.
Crystal Structure	Face Centered Cubic.
Young's Modulus, Modulus of Elasticity	600 GPa.
Poisson's Ratio	0.25
Heat of Formation	80,750 Cal/mole. (3.5 eV/molecule).
Band Gap	3.35 - 3.45 eV

CHAPTER 2

X-RAY DIFFRACTION ANALYSIS

The x-ray region is a part of the electromagnetic spectrum lying between 0.1-100 A^0 wavelengths. According to the fundamental Quantum law, $E=hc/\lambda$ (where h is plank's constant, c is velocity of light in vacuum and λ is wavelength), such shorter wavelengths means high energy, multi-layer penetration. Since the discovery of x-rays, many studies were conducted on the use of x-rays for understanding the chemical and physical properties of materials.

What makes x-rays unique for the study of material is their wavelength. The wavelengths of x-rays are in the order of spacing between the atoms in solids. Thus, by studying how x-rays are diffracted and scattered when they interact with materials, a prediction how atoms are arranged in crystalline compounds can be made.

2.1 X-Ray Diffraction

2.1.1 Interaction of X-Ray with Material

Let us study how an x-ray behaves when a monochromatic beam of x-rays falls on the surface of the crystal.

Single Particle

When a wave interacts with a single particle, the particle scatters the incident wave uniformly in all directions as shown in Figure 2.1

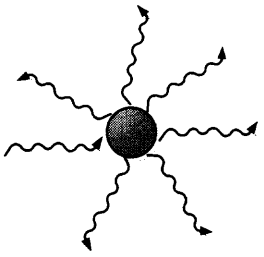

Figure 2.1 X-rays after hitting the atom scattered in all directions.

Solid Material or Crystal

A crystal is made up of atoms or molecules in a regular pattern in space. It is this regularity which is responsible for the diffracted waves. But if the arrangement of atoms was random, then the scattered waves would randomly add or cancel with each other.

One Atomic Layer

Figure 2.2 shows a coherent beam of radiation falling on the surface at an angle $Theta_{in}$. Of this beam few rays hit the atoms, few get scattered and few pass through the lattice spacing. Let us consider two such scattered waves A and B. Since the two beams are a part of the same original beam, they are in phase on reaching the crystal. If they travel the same distance, i.e. x=y and if the incoming angle is equal to the outgoing angle, then they reinforce each other giving a diffracted beam. This is also known as Bragg's Law I.

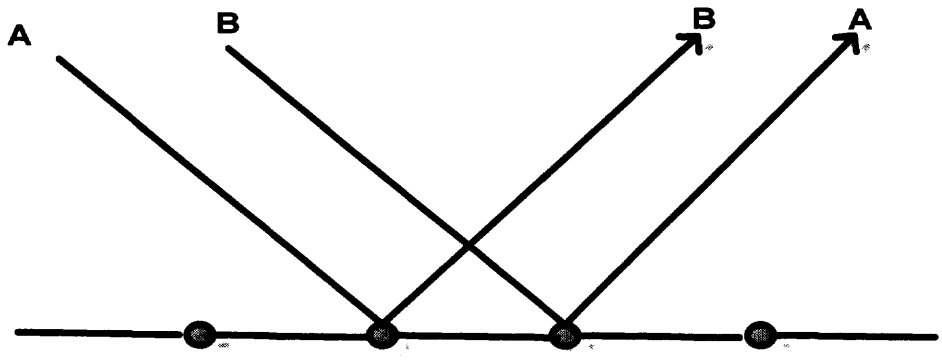

Figure 2.2 Rays A and B diffracted by two atoms on the same layer.

Two Atomic Layers

As in Figure 2.3, let us imagine that the radiation coming from a coherent source falls at an angle $Theta_{in}$ to the surface; some of the rays falls on the top plane and some on the second plane. Let us consider two such beams A and B. The two beams are in phase on reaching the crystal and they interact constructively reinforcing each other only when the distance traveled by beam A is equal to beam B or if the extra distance abc is a whole number of the wavelength. This is called Bragg's Law II.

According to Bragg's Law II, the coherence occurs only when $abc=n\lambda$. Using simple trigonometry it can be shown that $n\lambda= rdSin[Theta]$, where d is the distance between two layers, λ is the wavelength of incident light, Theta is the angle of incidence of the coherent beam, r is a perpendicular from first layer to ray B as shown in Figure 2.3. and n is an integer [22].

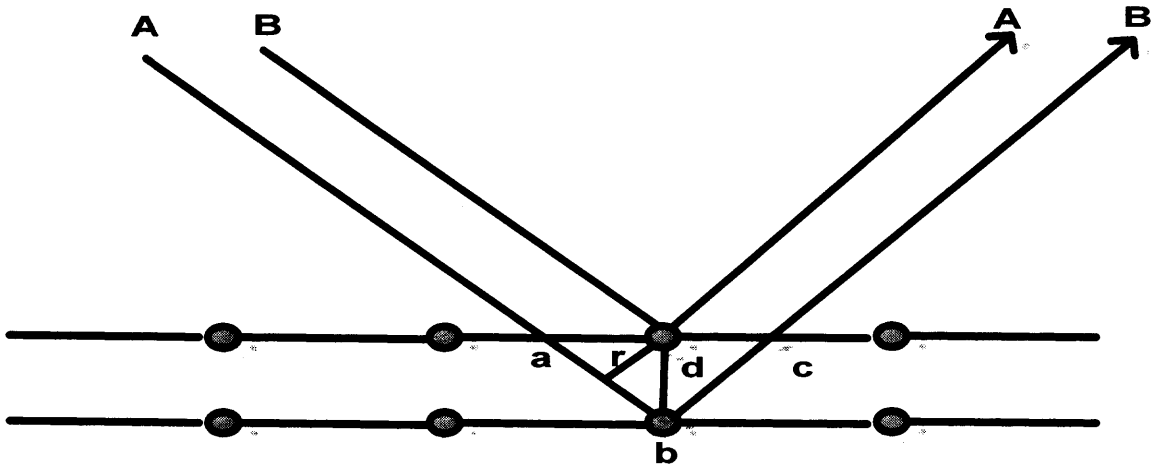

Figure 2.3 Ray A and B diffracted by atoms on different layers.

Reciprocal Lattice

Re-arranging the Bragg's Law in the form SinTheta = nλ/2 (1/d). It can be seen that SinTheta is inversely proportional to d- the interplanar spacing between the crystal lattice. Since, Theta is a measure of the deviation of the diffracted beam, it is obvious that the structures with a larger "d" will have compressed diffraction patterns and is opposite for structures with a small d.

Interpretation of x-ray diffraction patterns will be facilitated if the inverse relation between "SinTheta" and "w" can be replaced by a direct relation. This can be achieved by constructing a reciprocal lattice based on 1/d.

2.1.2 X-rays and Fourier Transforms

Studies show that the diffraction patterns are related to the object diffracting the waves through a mathematical operation called Fourier transform. Fourier transform of the scattered waves in the Figure 2.4 for single atom is as shown in the Figure 2.4 (a) the intensity drops off continuously with increasing scattering vector. Similarly Fourier transforms for two atoms is shown in Figure 2.4 (b). These transforms are unique for each material.

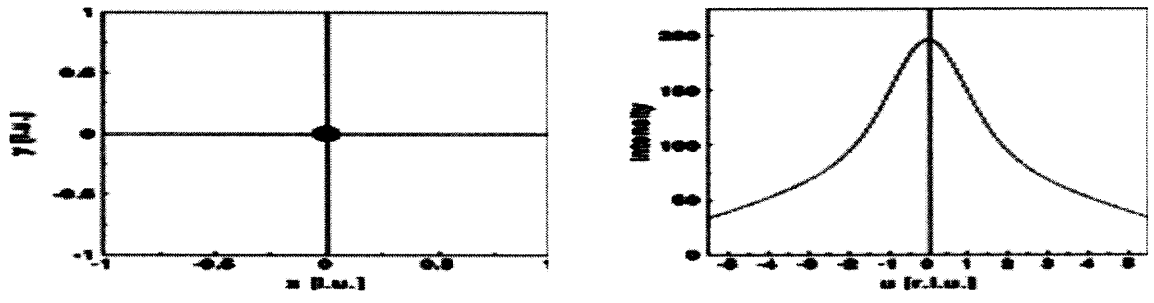

a

Figure 2.4 Fourier transforms for single atom (a) Fourier transforms for two atoms (b).

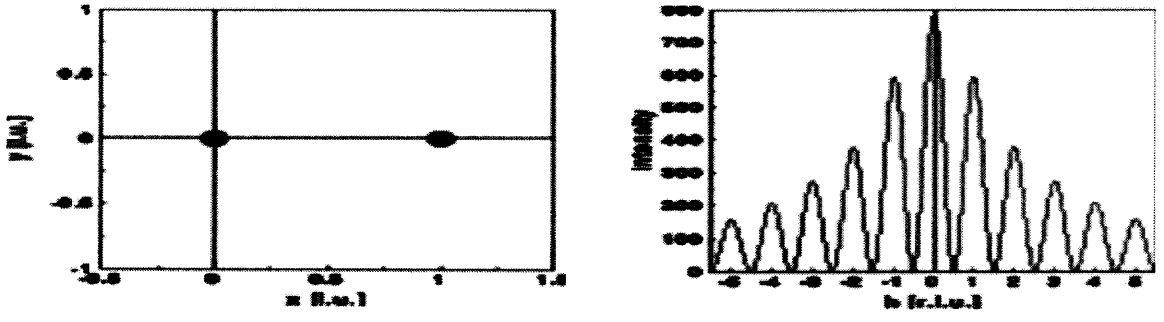

b

Figure 2.4 Fourier transforms for single atom (a) Fourier transforms for two atoms (b) (continued).

2.1.3 X-ray Setup

For diffraction to occur, it is necessary to satisfy Bragg's Law. An arbitrary setting of a single crystal in an x-ray beam will not generally produce any diffracted pattern. Hence, there would be little or no information in the diffraction pattern using monochromatic radiation. This problem can be solved either by using x-rays with large range of wavelengths or by rotating the crystal about its own axis. In later case, the x-rays are incident along an axis normal to the sample surface. As the sample rotates, the lattice planes will at some point make the correct Bragg angle for the monochromatic incident beam resulting in a diffracted beam.

The set up x-ray diffraction can be put into three basic units.

1. A source of radiation- x-ray tube along with high voltage generator.
2. Diffractometer.
3. Detector and counting system.

2.2 X-Ray Diffraction Analysis of the Sample

2.2.1 Sample Preparation

X-ray analysis of the TiN on substrate was done using Philips PW 3040 XRD instrument with Cu Kα radiation. Sample was cleaned thoroughly with IPA and dionized water before analysis, as traces of grease and/or finger prints can shift the spectrum significantly. The reference peaks for Ti and TiN under control conditions are as shown

in Figure 2.5 and Figure 2.6. These plots were taken from X-pert high score library (closely matched plots after pattern match).

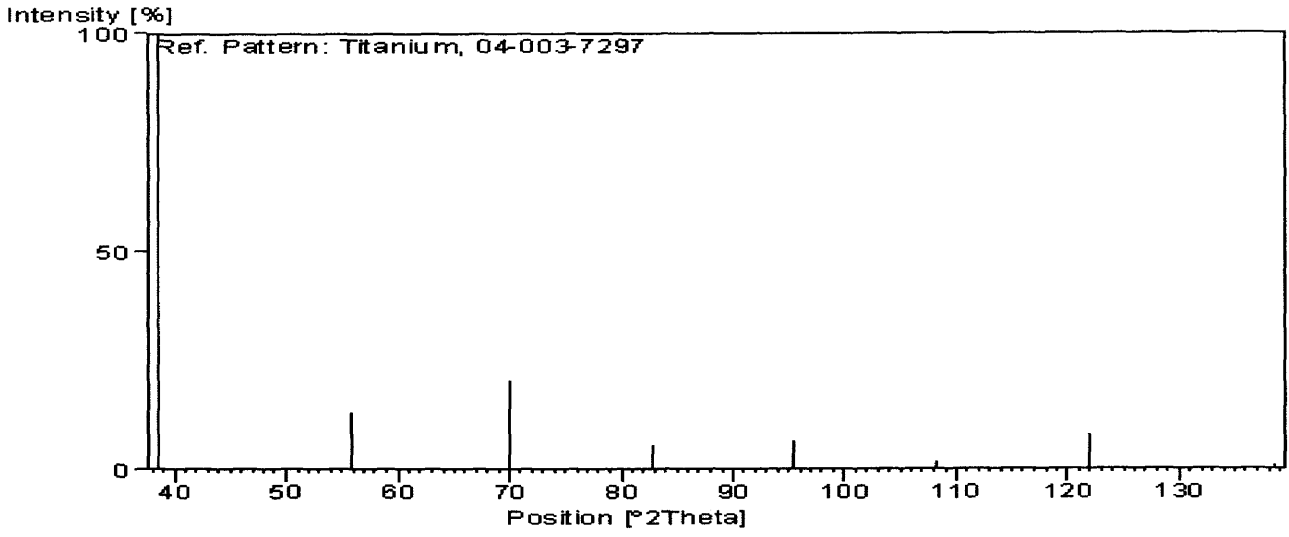

Figure 2.5 Reference diffraction lines for titanium.

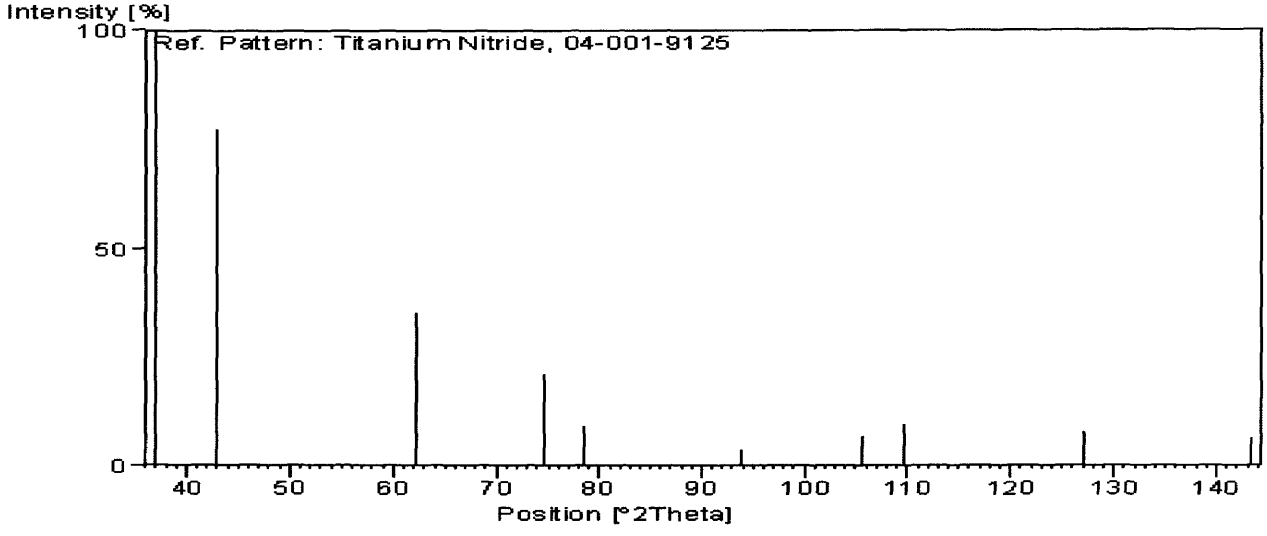

Figure 2.6 Reference diffraction lines for titanium nitride.

Two samples with TiN sputtered under different conditions were prepared for XRD analysis. XRD parameters for first round and second round of sample are:

Table 2.1 Scan Parameters for First Round of TiN Sputtering

Start 2Theta	15	End 2Theta	140
Step Size [2Theta]	0.02	Scan Speed	1.35s
KV	45	mA:	40

Table 2.2 Scan Parameters for Second Round of TiN Sputtering

Start 2Theta	20	End 2Theta	145
Step Size	0.02	Scan Speed	1.35s
KV	45	mA:	40

And all other parameters like temperature (25^0C), anode material (Cu), etc. were kept exactly same for both runs. The start 2Theta and stop 2Theta are selected by looking at the standard diffraction lines for Ti and TiN.

2.2.2 Results

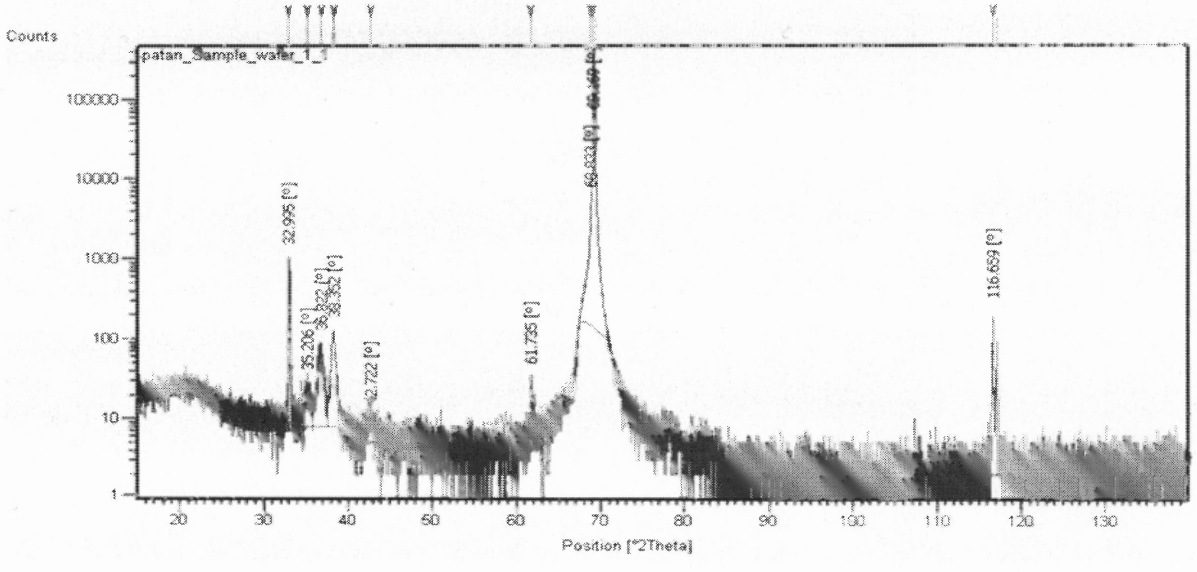

a

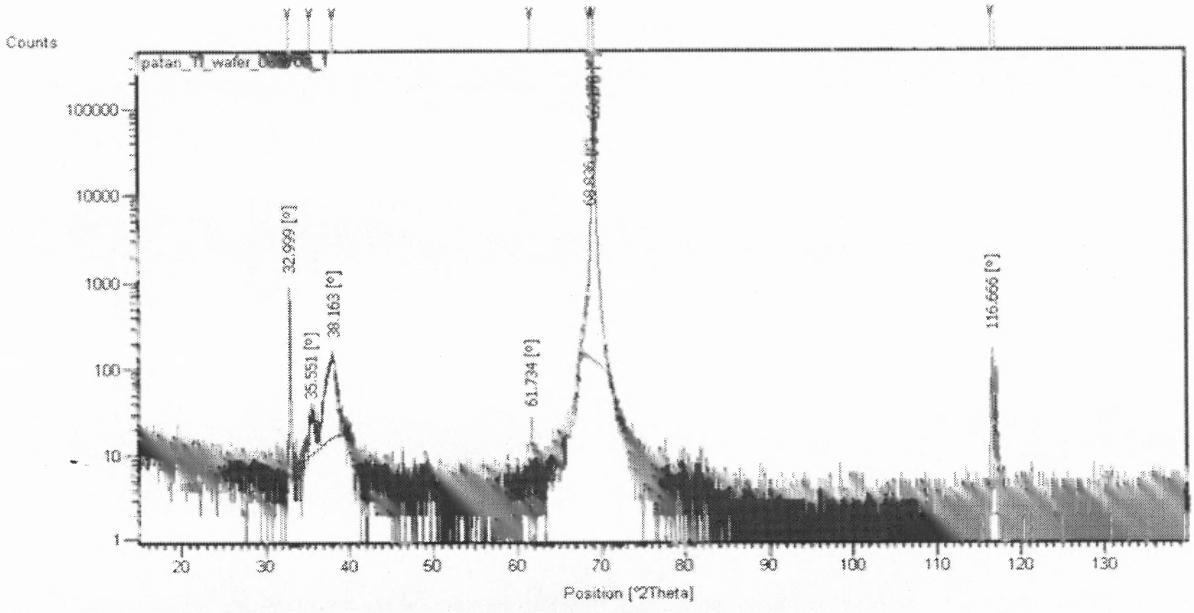

b

Figure 2.7 Diffraction peaks for (a) Sample (b) Ti on wafer (c) just silicon wafer.

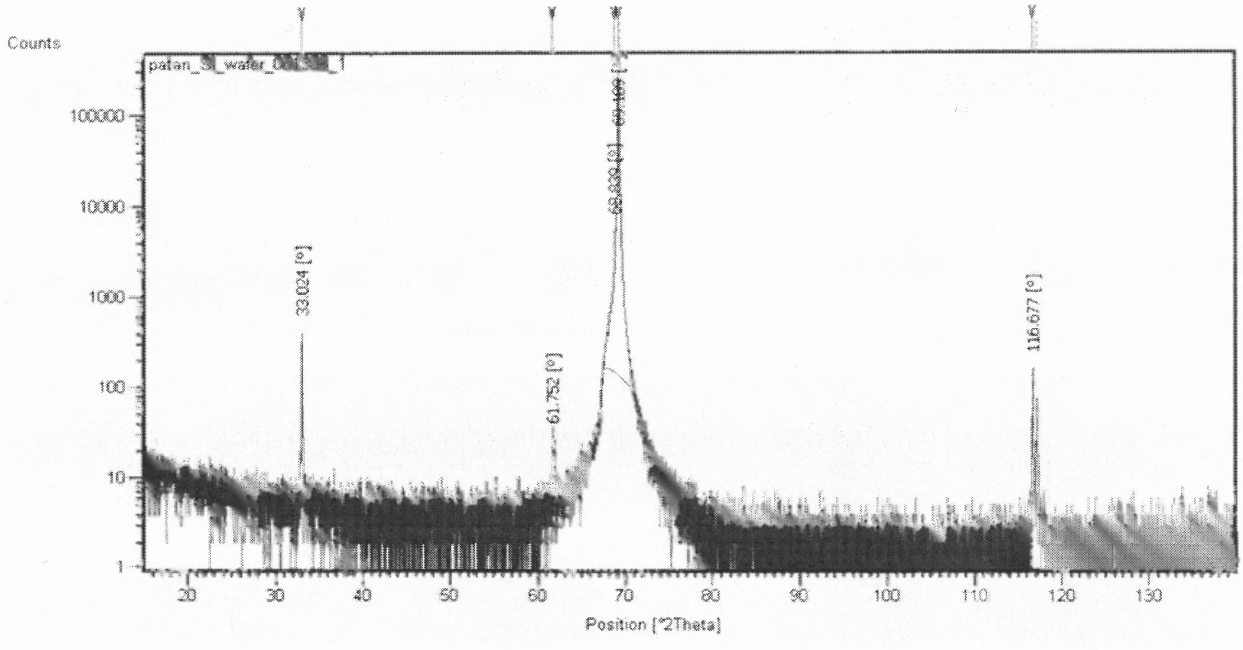

c

Figure 2.7 Diffraction peaks for (a) Sample (b) Ti on wafer (c) just silicon wafer (continued).

In Figure 6.1 (a) Shows diffraction pattern for sample, with peak positions at 2Theta=33^0, 35^0, 36.8^0 38^0,42^0,61^0,68.8^0,69^0 and 116.5^0 (approximately), (b) Shows diffraction patterns for Ti on wafer, with peak positions at 2Theta=33^0, 35^0, 38^0,61^0 ,68.8^0,69^0 and 116.5^0 and (c)Shows diffraction patterns for just silicon wafer, with peak positions 2Theta=33^0, 61^0,68.8^0,69^0 and 116.5^0.

Sample has all the diffraction peaks (2Theta=33^0, 35^0, 36.8^0 38^0,42^0,61^0,68.8^0 ,69^0 and 116.5^0), these peaks positions match exactly with the peak positions in standard diffraction peaks for TiN, Ti and Silicon (see Figure 1.2.). The peaks at positions 2Theta= 36.8^0 and 42^0 are missing in diffraction patterns for Ti on wafer (Figure 6.1(b)) as they correspond to TiN only. Similarly the peaks for angle 2Theta = 35^0, 36.8^0 38^0 and 42^0 are missing in diffraction patterns for just silicon wafer (Figure 6.1 (2.c)) since these peaks correspond to Ti and TiN only. This analysis and the presence of Ti and TiN peaks exactly at positions as in the standard diffraction peaks prove the presence of Ti and TiN. Other peaks at positions 2Theta= 61^0,68.8^0,69^0 and 116.5^0 in diffraction patterns for sample are due to the presence of Silicon and its compounds.

Table 2.3 Shows Peak Positions and their Presence

	Peak Positions 2Theta							
	33^0	35^0	36.8^0	38^0	42^0	61^0	68.8^0	116.5^0
Just Silicon Wafer	Yes	No	No	No	No	Yes	Yes	Yes
Ti on Wafer	Yes	Yes	No	Yes	No	Yes	Yes	Yes
Sample	Yes	Yes	Yes	Yes	Yes	Yes	Yes	Yes

CHAPTER 3

ATOMIC FORCE MICROSCOPY

Atomic Force Microscopy (AFM) is a technique used for the study of colloidal properties of surfaces. AFM works on the principle of cantilever beam. A micro cantilever beam probes sample surface with a sharp tip, protruding normal to the surface of the beam. Cantilever beam usually has a spring constant of 0.1 to 3N/m hence an AFM can measure a force range of the order of 10^{-6} to 10^{-9} N. A schematic of typical AFM setup is as shown in Figure 3.1.

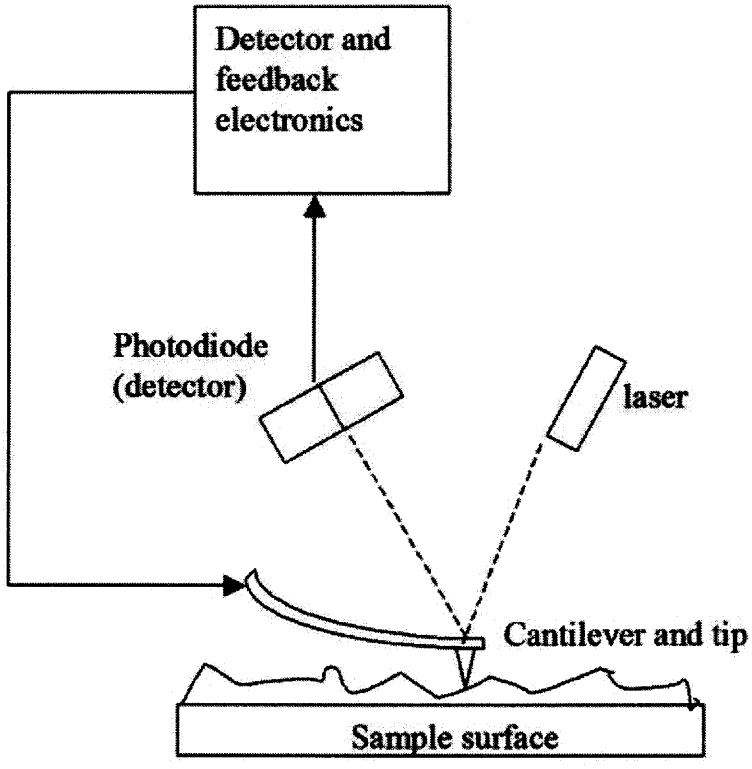

Figure 3.1 A typical contact mode AFM. The shift in the reflected laser beam is proportional to deflection of the cantilever beam. Detector and feedback electronics are used to correct the deflection.

Modes of Operation

The AFM studies can be split into three popular modes of operations: In contact mode, the separation distance between the tip and the sample is small and the detected force is the result of core-core repulsion. The contact mode can provide a resolution of the order of atoms, provided the surface is rigid. In non-contact mode, the separation between the tip and the surface is significant and the detected forces are the Vander Waals forces. The spatial resolution of the non-contact mode AFM is poor as compared to the contact mode AFM. However, non-contact mode AFM is less susceptible to imaging artifacts resulting from deformation of the surface by the tip. In order to have the resolution of contact mode and overcome the limitation of image artifacts, a third mode called tapping mode AFM is evolved. In this mode, the cantilever is forced to hover at a certain frequency over the surface. A change in the resonant frequency of the cantilever will result in a change in the amplitude of oscillation, which is directed by the laser- PSD system. When this happens, the feedback control lowers the sample so that the original amplitude of the cantilever is restored. Figure 3.2 shows the relationship between inter atomic force and separation distance.

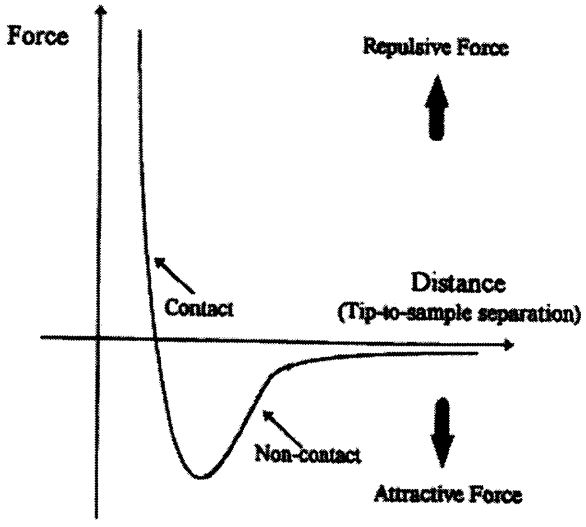

Figure 3.2 The curve shows the relationship between inter atomic force and separation distance.

As discussed previously in contact region the separation between sample and tip is few angstroms and the forces are repulsive. In non-contact region the tip is held in the order of tens to hundred angstroms above the sample and the interatomic forces are long-range Vander Walls forces (attractive).

3.1 Understanding the Data

3.1.1 Roughness Average (R_a)

It is defined as the ratio between the integral of the absolute value of the roughness profile height over the evaluation length.

$$Ra = 1/L \int_0^L |r(x)| dx .$$

Graphically the average roughness is the sum of the absolute values of the shaded region over the length 'L' as shown in the Figure 3.3.

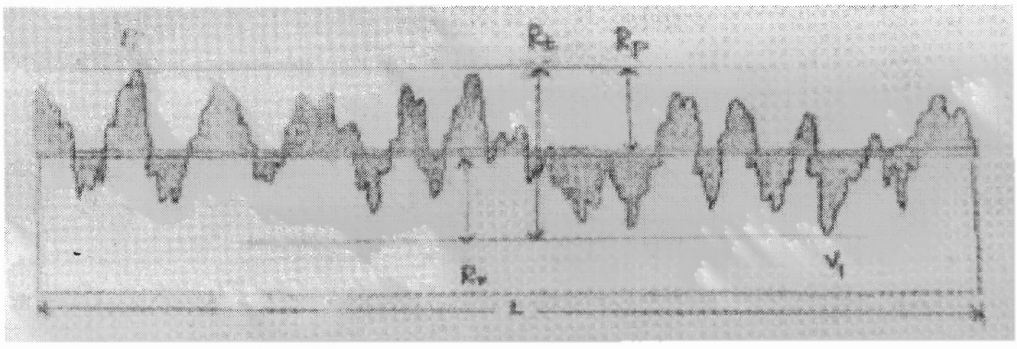

Figure 3.3 L is the evaluation length shaded area represents evaluation area, P_1 is the highest peak and V_1 is the deepest valley.

3.1.2 R_q- Root Mean Square Roughness

The root mean square roughness is calculated by using the formula

$$Rq = \sqrt{1/L \int_0^L r^2 (x) dx}$$

R_q and R_a are used as synonyms of each other.

R_q is proportional to R_a; it's about 1.11 times larger than R_a.

R_q is used mostly in optical applications where it is more directly related to the optical quality of a surface.

3.1.3 R_t, R_p and R_v

The peak roughness R_p is the height of the highest peak in the roughness profile over the evaluation line. R_v is the depth of the deepest valley in the profile and R_t (Rmax) is the sum of these two or the vertical distance from the highest peak to the deepest valley. Figure 3.3 illustrates these parameters.

3.2 AFM Analysis of Sample

3.2.1 Roughness Analysis

Roughness analysis of TiN sputtered substrate was carried using contact mode Digital Instruments, Nanoscope AFM. A piece 2mm × 2mm area was cut from the wafer. Sample was cleaned for any grease using Iso Propane Alcohol and then with distilled water. Keeping in mind roughness to be expected, cantilever beam of appropriate tip size was selected. Two rounds: first with 3μm × 3μm plane area over the TiN pads and second with 100μm × 100μm across the interface between the substrate and TiN layer with scanning parameters as: Scan rate 0.9537 Hz and Data scale 80nm were run.

First run:

A.

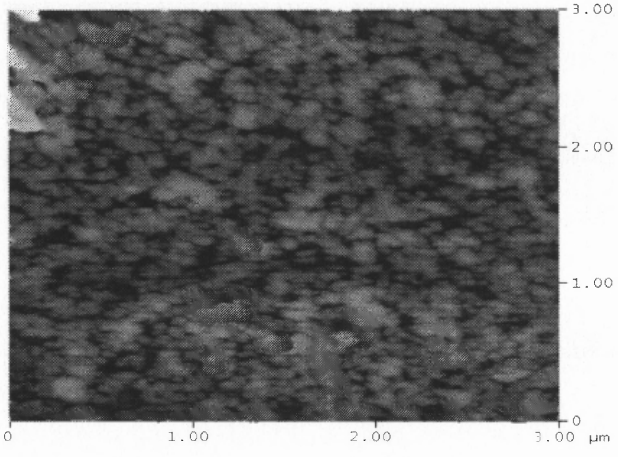

Figure 3.4 Roughness profile of a plane 3μm × 3μm surface area over the TiN coated electrodes. (A) shows top view of surface and (B) oblique of the same image, peaks and valleys are clearly seen in this view.

B.

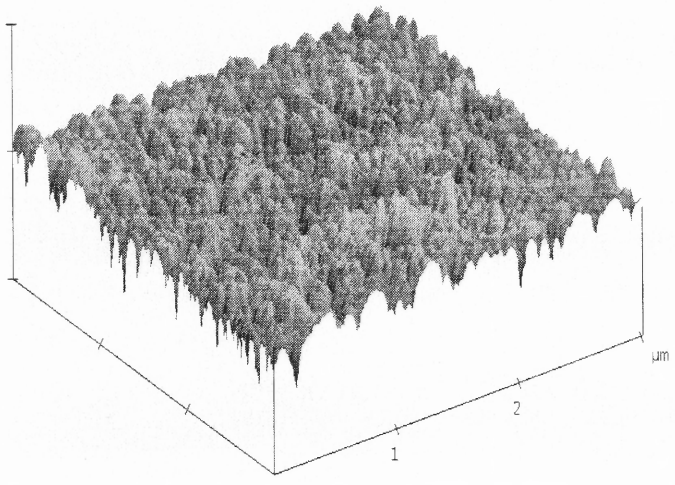

Figure 3.4 Roughness profile of a plane 3µm × 3µm surface area over the TiN coated electrodes. (A) shows top view of surface and (B) oblique of the same image, peaks and valleys are clearly seen in this view (continued).

Table 3.1 Image Statistics of Scand Area is Summarized as Follows

Img. Z range	7.496 nm
Img. Mean	0.117 nm
Img Raw Mean	27.468 nm
Img. Rq	7.903 nm
Img. Ra	6.175 nm
Img. Rmax	76.660 nm
Img. Srf. Area	9.806 μm^2
Img. Prj. Srf. Area	9.000 μm^2
Img. Srf. Area diff	8.952 %

B.

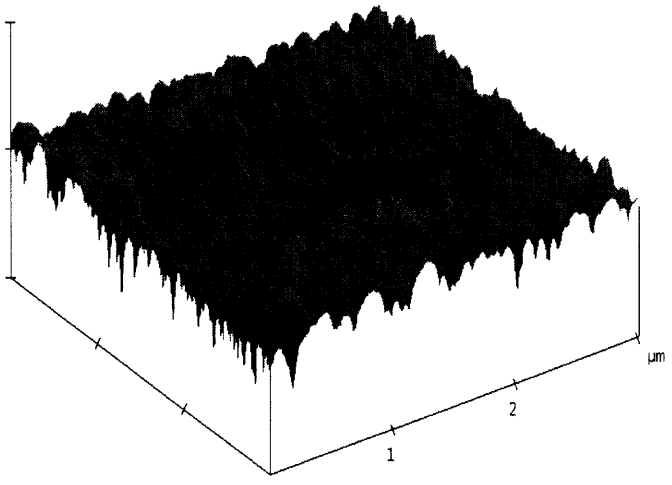

Figure 3.4 Roughness profile of a plane 3µm × 3µm surface area over the TiN coated electrodes. (A) shows top view of surface and (B) oblique of the same image, peaks and valleys are clearly seen in this view (continued).

Table 3.1 Image Statistics of Scand Area is Summarized as Follows

Img. Z range	7.496 nm
Img. Mean	0.117 nm
Img Raw Mean	27.468 nm
Img. Rq	7.903 nm
Img. Ra	6.175 nm
Img. Rmax	76.660 nm
Img. Srf. Area	9.806 μm^2
Img. Prj. Srf. Area	9.000 μm^2
Img. Srf. Area diff	8.952 %

3.2.2 Section Analysis

Thickness of TiN is estimated by scanning across the interface. Offline section analysis was done on data from the second run. Figure 3.5 summarizes the analysis. A section line is drawn with an angle across the interface, two points one on the substrate and other on the TiN layer is selected and are moved alternately along the horizontal axis to find maximum vertical distance. For a scan angle of 16.959 ^{0} and horizontal distance of 3.516 μm, maximum vertical distance was 1.072 μm. Hence an approximate TiN thickness is 1 μm.

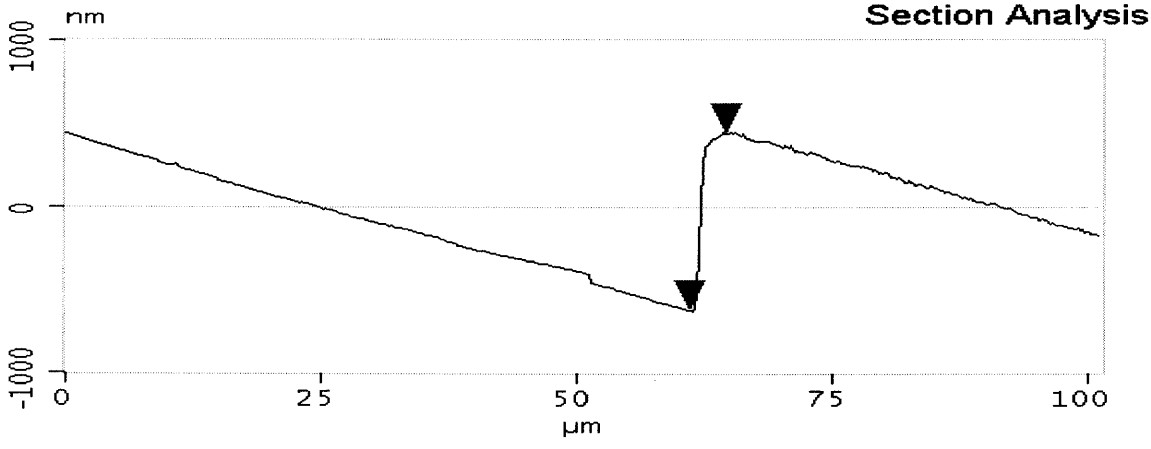

(a)

Figure 3.5 Shows section analysis. (a) and (b) shows the section line across, red triangles can be moved to find maximum vertical distance. (c) shows three dimensional roughness profile of the same image, a clear difference between these two entities is seen in this view.

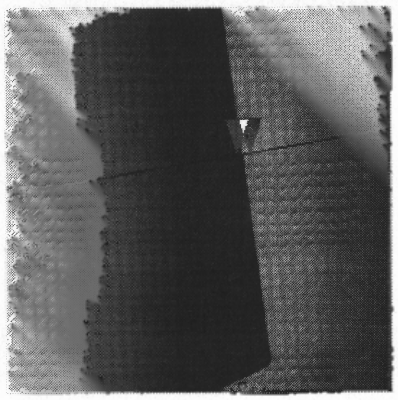

(b)

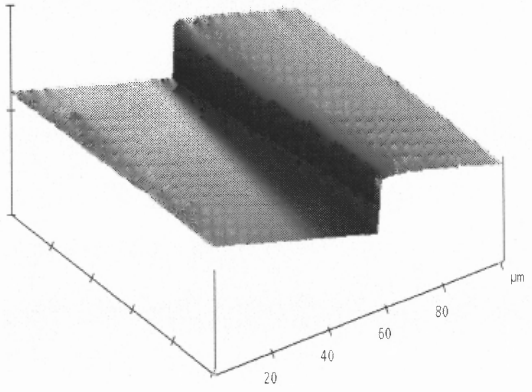

(c)

Figure 3.5 Shows section analysis. (a) and (b) shows the section line across, red triangles can be moved to find maximum vertical distance. (c) shows three dimensional roughness profile of the same image, a clear difference between these two entities is seen in this view (continued).

Measurements by detecting change in resonant frequency due to accumulation of mass on a piezoelectric crystal performed during sputtering in clean room suggested a thickness of 800nm.

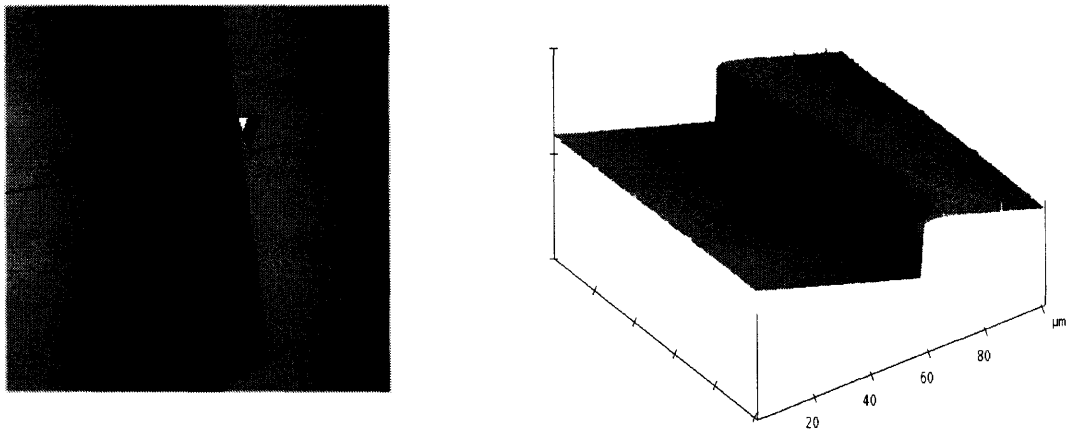

(b) (c)

Figure 3.5 Shows section analysis. (a) and (b) shows the section line across, red triangles can be moved to find maximum vertical distance. (c) shows three dimensional roughness profile of the same image, a clear difference between these two entities is seen in this view (continued).

Measurements by detecting change in resonant frequency due to accumulation of mass on a piezoelectric crystal performed during sputtering in clean room suggested a thickness of 800nm.

CHAPTER 4

FABRICATION PROCEDURE

4.1 Thin Film Deposition Techniques

4.1.1 Plasma Enhanced Chemical Vapor Deposition

Plasma Enhanced Chemical Vapor Deposition (PECVD) or Plasma Assisted CVD (PACVD) is a special case Chemical Vapor Deposition (CVD). CVD can be defined as the deposition of solids on the surface from a chemical reaction. This process takes the advantage of formation of solid materials during chemical reactions between reactants in gas phase or liquid or with the substrate material. CVD is a popular technique in semiconductor industry as high deposition rates and thick coating can be readily achieved, moreover CVD equipment is relatively simple. The negative side of CVD is, CVD is productive at temperatures 600^0C and above [23,24], where thermal stability of the substrate and other metal coatings (Aluminum) may limit its applicability. Hence (PECVD) or (PACVD) is used as an alternative. In PECVD the reaction is assisted by creation of plasma in the chamber. As a result, the substrate temperature can be kept considerably low [25,26].

As the temperature of gas is increased, the atoms are gradually ionized, that is there are stripped of their electrons and a plasma is formed which consist of Ions, electrons and atoms which are not ionized. Pressures close to vacuum are maintained in the chamber to increase ionization of plasma by reducing average distance traveled between collisions, as a results the collisions are more frequent and an improved rate of deposition is achieved [27,28,29].

PECVD is popularly used for deposition of oxides of silicon in the clean room. Silicon oxide (SiO_2) is formed when saline SiH_4 reacts with N_2O [30]. First, SiH4 decomposes to deposit Si on substrate as in polysilicon growth, producing H_2 byproduct. Then the deposited Si is oxidized by N_2O reaction, producing N_2 byproduct [31].

4.1.2 Physical Vapor Deposition

Physical Vapor Deposition (PVD) is a thin film technology used mostly for deposition of metals in the clean room. PVD is different from chemical vapor deposition in the sense that films are deposited automatically by means of flux of individual neutral or ionic species [32]. The most common methods of physical vapor deposition (PVD) of metals are evaporation, e-beam evaporation, plasma spray deposition and sputtering. Metals like ,Au Al, Cu and Ti are most commonly deposited using PVD. Evaporation occurs when a source material is heated above its melting point in an evacuated chamber. The evaporated atoms then travel at a high velocity in straight line trajectories. The source can be melted by resistance heating, by RF heating, or with a focused electron beam.

In ion beam sputtering, a source of ions is accelerated toward the target and ions impinge on its surface sputter some of the surface atoms, these sputtered ions get deposited onto the wafer which is placed facing the target. The ion current and energy can be independently adjusted. Since the target and the wafer are placed in a chamber that has lower pressure, more target material and less contamination are transferred to the wafer.

Many other techniques are employed to increase the ion density and hence the sputter deposition rate, like using a third electrode that provides more electrons for ionization or the use of magnetic field, such as ECR (Electron Cyclotron Resonance) to capture and spiral electrons, increasing their ionizing efficiency in the vicinity of sputtering target.

The material we wish to sputter is made as target which is biased at high negative voltage. Argon gas is introduced into the chamber at some pressure. The role of the electric field is to accelerate an electron which in turn collide with argon, breaking some of argon atoms into ions and more electrons. When these ions hit the target they may sputter some of the target atoms, these sputtered atoms fly off randomly in all directions, and some of them land on the substrate- condense and form a thin film. The phenomenon of sputtering is summarized in the Figure 4.1.

A special technique called reactive sputtering is used for deposition of compounds; reactive gases are introduced into sputtering chamber during deposition allowing material sputtered from the target to combine with gasses forming chemical compound films. The reaction could take place at target, in the gas phase or at surface of the substrate [33].

Sputtering is essentially involves knocking out atoms off the surface of a film by impact of ions, hence it is also used for removal of metals or for etching.

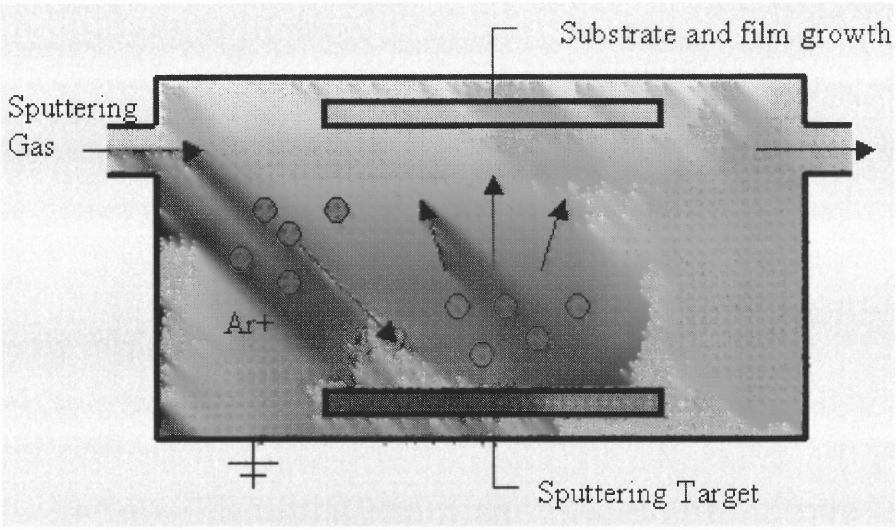

Figure 4.1 The phenomenon of sputtering in side a sputtering chamber is shown [34].

PVD and PECVD both have there pro and cons. The choice of the process is governed by the achievability of reacting species in the chamber to deposit required material in least time with defined quantity and quantity.

4.1.3 Electron Beam Evaporation

Electron beam (e-beam) evaporation is also an evaporation technique in which the material to be coated (source material) is placed in crucible. The source material is then heated using electromagnetically accelerated particle beam of electrons with inherently high density of energy which are focused over very small area, this results in local melting and evaporation of the source material. A schematic of e-beam evaporation system is as shown in Figure 4.2. Vacuum pressures are maintained in the chamber to facilitate free molecular evaporations and subsequent condensation on all surfaces.

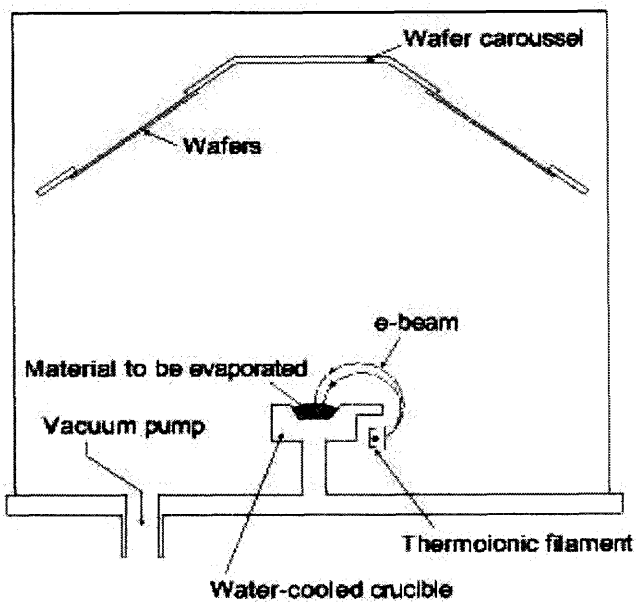

Figure 4.2 A typical electron beam setup [35].

Thermal emission of electrons from a tungsten filament biased to a negative potential with respect to a collimating slit is typically the source of electrons. e-beam is guided on to the metal using a deflecting magnet. The source of e-beam is kept bellow the crucible as shown in the Figure 4.2 to minimize contamination.

4.2 Lithography

Lithography is the key to planner processing. The process of selectively removing material to transfer patterns on to the substrate is achieved by spin coating the substrate with a light sensitive material called photoresist. Photoresist is a radiation sensitive compound that can be classified as positive or negative depending on how it responds to radiation. For positive resists, the exposed regions become more soluble and are thus easily removed in the development process. The net result is that the patterns formed in the positive resist are the same as those on the mask. For negative resist, the exposed

regions become less soluble and the patterns formed in the negative resist are the reverse of the mask patterns. Positive photoresist consist of three components: a photo sensitive compound, a base resin and an organic solvent. Negative photoresist are polymers combined with photo sensitive compound. After exposure the photo sensitive compound absorbs the optical energy and converts it into chemical energy to initiate polymer cross linking reaction. The cross linked polymer becomes insoluble in developer solution. One very common positive photoresist used is based on a mixture of Diazonaphthoquinone (DNQ) and Novolac resin (a phenol formaldehyde resin). One very common negative photoresist is based on epoxy based polymer. The common product name is SU-8 photoresist.

Positive photoresist Developer is hydrated alkaline material which dissolves readily in water, giving a buffered alkaline solution for economical development of novolac polymer films used in micro imaging.

UV light is used to expose the wafer protected by a mask which has features to be transformed on to the substrate. UV light polymerizes the photoresist by breaking inter molecular chains, making them readily soluble in organic solvents (developer)

4.3 Wafer Clean

Cleaning is a critical step in enhancing the yield for a semiconductor process. Cleaning depends up on finding a cleaning agent with greater affinity for contaminants then the surface being cleaned. The common contaminants on the silicon substrate are grease, dust particles, left over from previous process (e.g.: photoresist) and static charge (ions). A sequential three step procedure is used frequently in the clean rooms for primary cleaning

of substrates. Is Propane Alcohol (IPA) to remove any grease due to improper handling, followed by acetone to remove any organic contaminants and finally with deionized water to rinse IPA , Acetone and also a to remove any static ions. A more rigorous cleaning using acids and strong organic solvents is used as the fabrications steps mature and demand.

4.4 Fabrication of Electrodes

The mask design is done using Mentor Graphics IC station Version 8.4. Mask are made of soda lime with chrome coating and had critical dimension of 5μm. Ten different electrodes five circular (d=10μm,20μm,40μm,80μm and100μm) and five squire (s= 10μm,20μm,40μm,80μm and100μm) with four channels each where designed. These set was repeated allover a 5" mask. The distance between the contact and bonding pads is at least 3 mm. Each bonding pad is 0.5 mm × 0.5 mm in area. There are total three masks. The layout of each mask is shown in Appendix.

The first mask is a clear on black type of mask; patterns on this mask are used for depositing Ti as a first layer. Dimensions on this mask are one unit more than the required dimensions for each electrode.

The second mask is also a clear on black type of mask. This mask is used to sputter TiN only on the contacts. The features on this mask are corresponding to features on the first mask in size.

The third mask is a black on clear type of mask. This mask is for opening windows only for contacts and bonding pads and covering rest of the wafer with silicon oxide. The dimensions of the features on this mask are exactly same as required for each

electrode. Patterns consisting of cross, rectangle and, an L shape are made on the mask and are used as alignment marks for subsequent layers.

Fabrication of electrodes was carried out in the class 10 clean room at NJIT. The starting material was p-type, 5'', single side silicon oxide coated <100> silicon wafer with 500μm thickness.

First step was to deposit titanium as a base metal for electrodes. Using mask one required pattern was transferred on to substrate as described. Substrate was cleaned first with Is propane alcohol (IPA), then with acetone followed with deionized water rinse. After dehydrating the wafer at 120^0C on a hot plate, primer was spread across the wafer at an a speed of 800 rpm for one minute followed by photoresist at a speed of 1000 rpm for one minute which would correspond to a resist coat thickness of 1.5 μm. Later wafer was pre-backed at 110^0C before placing it in a mask a-liner. UV light at 15mW for 25 sec was used for exposing the wafer. Then the wafer was agitated in developer and deionized water alternately till sharp edges were visible under the microscope. Finally it was post backed at 120^0c before sending the wafer for metal layer deposition using electron beam vaporization.

Titanium (Ti) was deposited as a base layer using e-beam vaporization machine. With chamber set to vacuum pressures, 99.9% pure Ti pallets where filled into the crucible up to ¼ mark. The system was water cooled at 50^0F, with pressure inside the chamber as 2×10^{-6}torr a deposition rate of $2A^0$/s was achieved. The distance between target and substrate was about foot and half. This set up run for 30 min. crystal measurements showed a thickness of around 1μm of Ti.

Ti coated wafer was dipped in acetone bath for Ti lift off. Altering wafer in acetone bath and in running water gave a thoroughly cleaned wafer.

The next step was to insulate the metal lines using silicon oxide coating; this was achieved by doing lithography as explained before with same parameters. A negative mask (black on clear) was used for protecting the contacts and bonding pads with a photoresist. After hard baking the wafer, it was introduced into oxidizing chamber. 400ccm saline and 900ccm of nitrous oxide at 25 kV of RF power was set. Target thickness of 1μm was achieved in 30 minutes for process pressure of 900mtorr, temperature in the chamber set to 120^0C. Oxide lift-off was done in an acetone bath for four to five hours for clearing the pads and contacts off the oxide film.

One more lithography step on oxide film to open window for titanium nitride (TiN) sputtering was done using mask II. Steps involved in order for lithography were; Spin coating of wafer with primer at 800 rpm for 1 minute, photoresist coat at 2000 rpm for 1mintue, soft baking of substrate at 110^0c, UV exposure at 15mW for 25 sec, developing, inspection and finally hard baking.

At this stage wafer was cut into two pieces, one piece was sent for TiN PVD and the other piece was used for Ti, CIC measurements. Photoresist coat on the wafer was used as insulation for Charge Injection Capacity (CIC) measurements.

Last step was to perform PVD of TiN, it was done using Varian DC 3125 machine. Hard backed photoresist was used as mask for TiN deposition only on contacts. TiN was spurted using a titanium target in an atmosphere of nitrogen (N_2) and argon (Ar) for two hours. Power was kept between 4900w – 5400w (I=7Amp; V=700 to770 volts). Efforts where made to keep N_2 and Ar pressure at 1:1 proportion, but resulted in arcing

inside the chamber. N_2 pressure at 1.2mtorr and Ar at 5.3mtorr was stable and resulted in deposition rate 2 A^0/sec (display value). Excess TiN was lift-off in an acetone bath as described previously. Figure 4.3 shows the schematic of wafer after each process step.

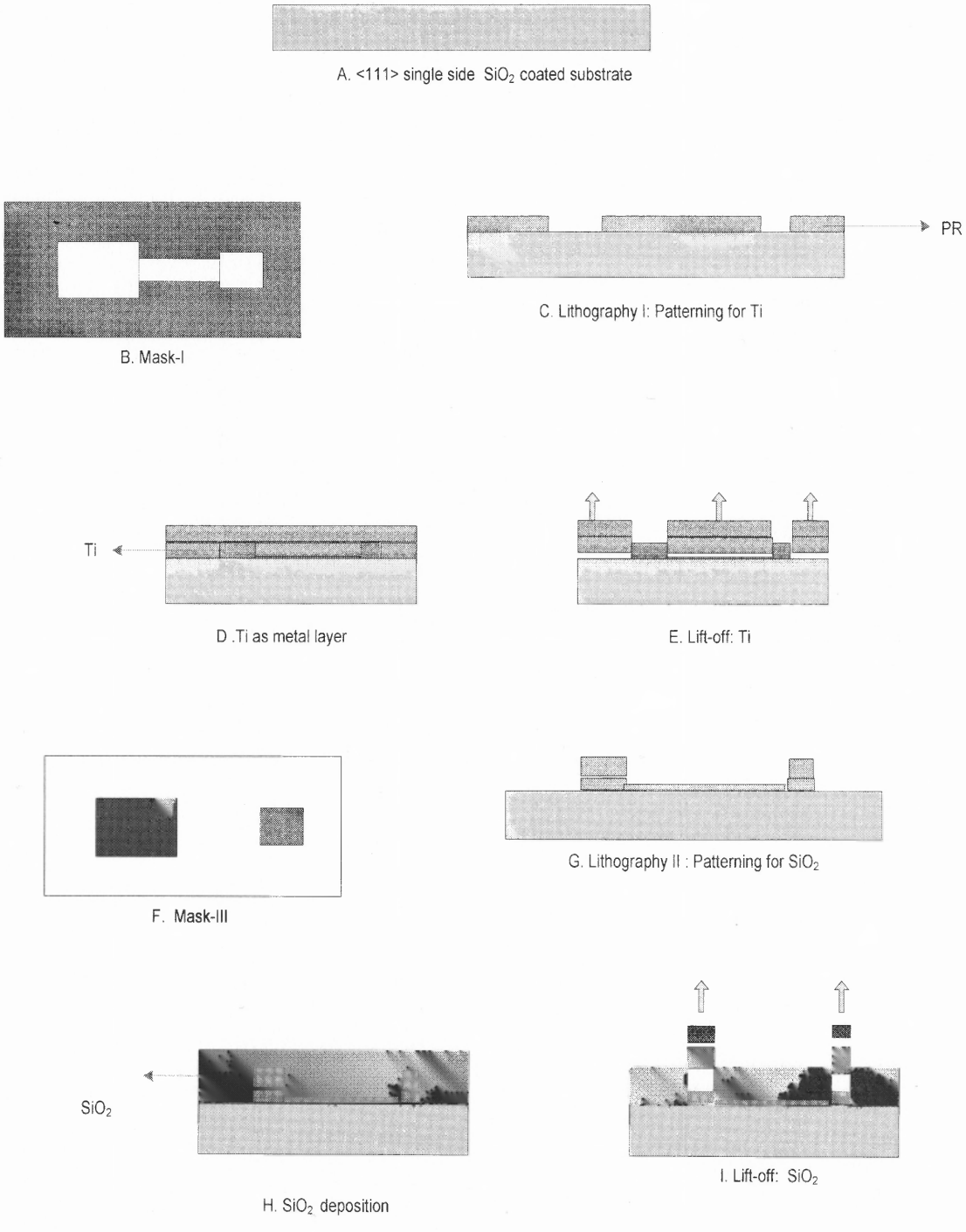

Figure 4.3 Schematic of wafer after each process step

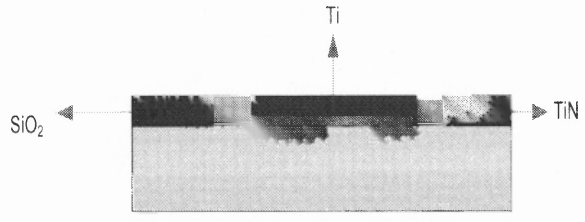

J.Pattern for Ti testing

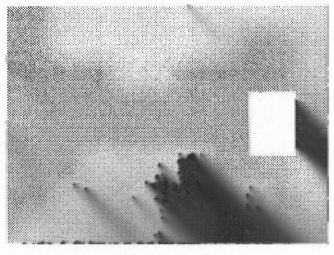

K. Mask-II

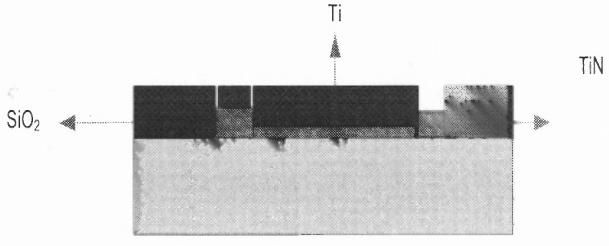

L. Lithography III : Patterning for TiN

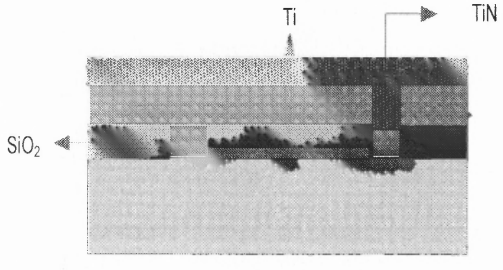

M. TiN sputtering.

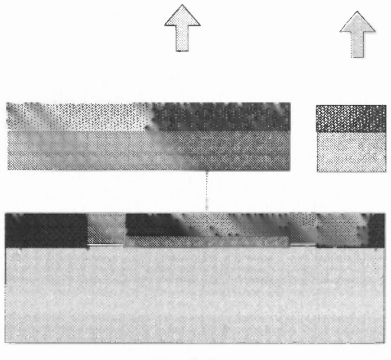

N. Lift-off: TiN

Figure 4.3 Schematic of wafer after each process step (Continued).

The sequence of steps for fabricating these electrodes can be summarized using following process flow.

- Wafer clean- IPA, acetone, deionized water; dehydrated at 120^0C.
- Photo lithography – Mask one, primer at 800 rpm for 1 minute, photoresist at 1000 rpm for 1 minute. Soft bake 110^0C, hard bake 120^0C.
- Metal deposition- Electron beam vaporization.
- Lift off- Ti.
- Wafer clean- IPA, acetone, deionized water, dehydrated at120^0C.
- Photo lithography- Mask two, primer at 800 rpm for 1 minute, photoresist at 1000 rpm for 1 minute. Soft bake 110^0C, hard bake 120^0C.
- Oxidation-Plasma Enhanced Chemical Vapor Deposition- SiH 400ccm, NO_2 at 900ccm, process pressure 900mtorr, temperature 120^0C, RF power 25kV, target thickness 1μm.
- Lift-off- Sio_2
- Wafer clean- IPA, acetone, deionized water, dehydrated at120^0C.
- Photo lithography- Mask three, primer at 800 rpm for 1 minute, photoresist at 1000 rpm for 1 minute. Soft bake 110^0C, hard bake 120^0C.
- Sputtering- Power 4900W-5400W (I=7Amp; V=700 to770 volts), pressure: N_2 at 1.2mtorr and Ar at 5.3mtorr, deposition rate 2 A^0/sec (display value).
- Lift-off- TiN.
- Wafer clean- IPA, acetone, deionized water; dehydrate 120^0C.

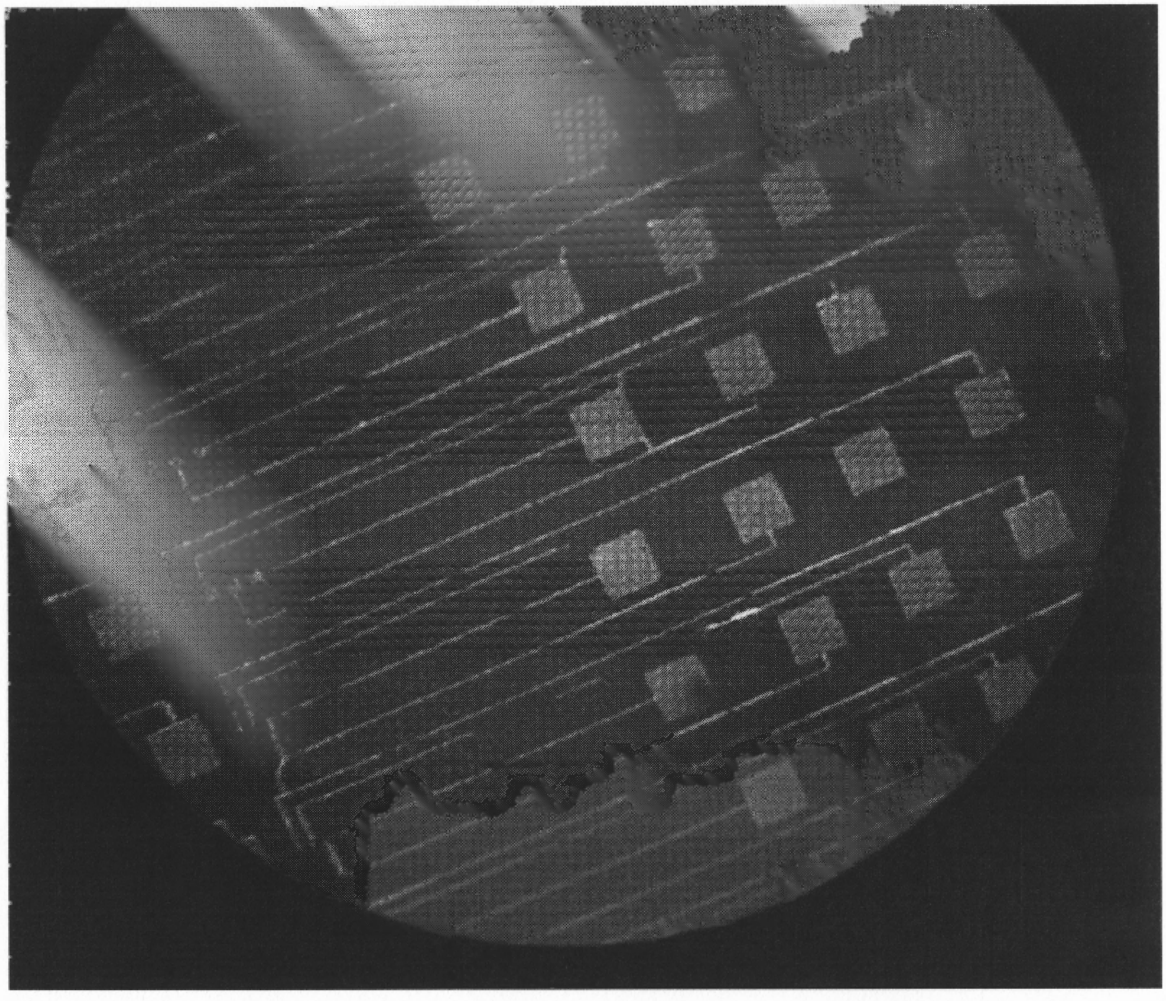

Figure 4.4 Image of the wafer with patterned electrodes of different size. The large squares are bonding pads and the small circular or square shapes are electrode contacts.

Figure 4.4 shows of the wafer with patterned electrodes of different size. The large squares are bonding pads and the small circular/square shapes are electrode contacts. The distance between bonding pads and contacts is at least 3mm. The contacts are at least 150 μm apart. A set ten different electrodes-five square and five circular were designed and are step-repeated allover the wafer with step size 300μm.

CHAPTER 5

CHARGE INJECTION CAPACITY

Many applications for neural stimulation demand high current densities from the electrodes to effectively active neural tissue [36]. Electrodes of micro scale are needed to localize the volume of activation and also to accommodate more on an array, specially in applications related to central nervous system, vision [37] etc. These pioneering techniques urge electrodes to be fabricated that are capable of handling larger current and higher charge densities. Electrodes made traditionally from noble metals like platinum and tantalum oxide or capacitor electrodes are not able to deliver such high current densities.

Microelectrode for neural stimulation is typically characterized by charge injection limit, which represents the maximum charge that can be injected into tissue without exceeding some practical set limits (typically defined as water window of hydrolysis) within which the electrode is considered to operate reversibly [38]. Reversibility of charge is critical, as pH shifts in biological environment due gas evolution, or introduction of by products, can potentially have adverse effects on the surrounding neural tissue [39,40] resulting tissue damage by increased cell death.

Charge injection into biological tissue is achieved through both faradaic and non-faradaic reactions at the electrode/tissue interface. Electrical stimulation of metallic electrodes in an aqueous electrolyte introduces charges into the environment via electrochemical reactions. At low intensities, charge injection is dominated by capacitive mechanisms [41]. With increasing current intensities, reversible and irreversible faradaic reactions may occur [42]. Almost all faradaic reactions produce or consume hydrogen or hydroxyl ions. Since the presence of these ions at the electrode surface alters hydrogen ion

concentration, one can expect stimulus induced pH shift. Stimulation parameters for neural prosthesis must be controlled to ensure minimal pH changes. [43]. Table 5.1 shows reactions associated with platinum electrode stimulation.

Table 5.1 Example of Reversible and Irreversible Electrochemical Reactions Associated with Platinum Electrode Stimulation [44]

Oxidation and reduction $Pt + H2O \Leftrightarrow PtO + 2H+ + 2e-$

Corrosion of electrode metal $Pt + 4Cl- \rightarrow [PtCl4]2- + 2e-$

Hydrogen generation $2H2O + 2e- \rightarrow H2(g) + 2OH$

Oxygen generation $2H2O \rightarrow O2(g) + 4H+ + 4e-$

Water hydrolysis is the most common electrical reaction during pulse stimulation, which limits charge injection capacity of the electrode. The potential range defined by hydrogen evolution at the cathode and oxygen evolution or surface oxidation at the anode is termed as water window of hydrolysis [45]. Experiments with TiN electrodes showed that the electrode potential range within which hydrogen absorption occurred before hydrogen gas evolution starts in the cathodic direction was observed as -0.75V to -1.25V and thereby the limit within which electrode is considered to operate reversibly for a cathodic pulse was determined as -1.0V conservatively. Figure 5.1 shows a typical cyclic voltammogram of a TiN coated electrode, no visible oxidation/reduction peaks are visible within the water window of - 1V to +1.2V. This suggests that if pulsed within water window, charge injection of TiN is through non-faradaic processes, i.e. mainly via capacitive mechanism. At the voltage higher than the water window potentials, the sharp increase in both cathodic and anodic current is due to the oxidation and reduction reactions, mainly water hydrolysis and gas evolution.

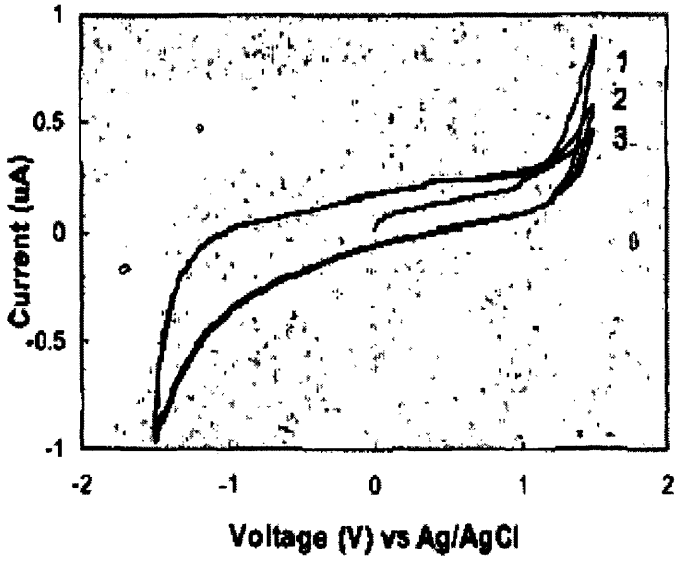

Figure 5.1 Cyclic voltammograms of a TIN electrode at a potential scan rate of 100 mV/s [46]

Reversibility of charge is achieved with the use of charge balanced waveforms. These current pulse waveforms retain overall zero net charge by employing rectangular geometry, with each pulse having cathodal and anodal components with current amplitudes and durations identical for the pulse, as shown in Figure 5.2. The importance of charge-balance is to avoid corrosion of an electrode or damage to tissue from the accumulation of electrochemical byproducts. A number of other strategies for achieving charge-balance using capacitor discharge or by shorting to a large-area counterelectrode have also been employed, All measurements are made using similar waveform shown in Figure 5.2.

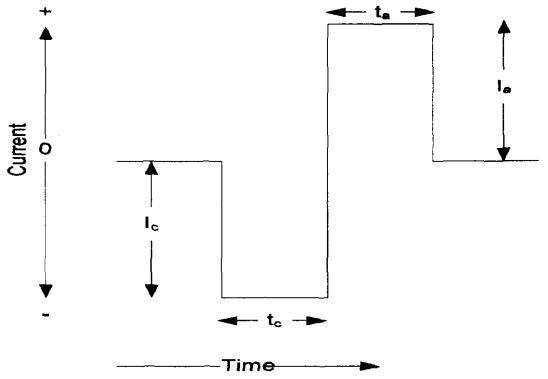

Figure 5.2 A typical bi-phasic, symmetric current pulse with charge balance (with zero net charge).Ic = cathode current Ia = anodic current tc= cathodic half phase period (0.5 ms), ta= anodic half phase period (0.5 ms) for charge balance Ic x tc =Ia x ta.

Michigan Electrodes were kindly provided by the Center of Neural Communication Technology, University of Michigan were used as reference for all measurements conducted on NJIT patterned electrodes. Fabrication of these electrodes is summarized in the following schematic.

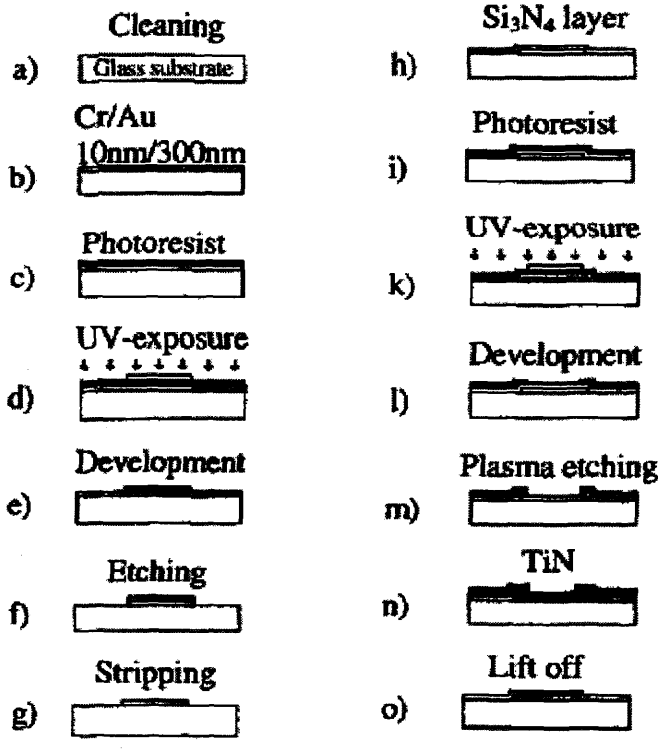

Figure 5.3 Thin film technology for the fabrication of microelectrode array.

The Figure 5.4 shows the real picture of 5 channel single shank micro electrode. Leads coming out of each channel are made of ploysilicon.

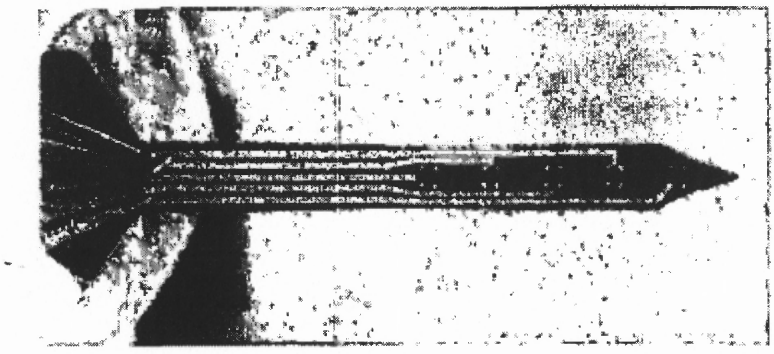

Figure 5.4 Real picture of 5 channel single shank micro electrode [47].

5.1 Surface Morphology and Charge Injection Capacity

For stimulating/ sensing electrodes, electrode-electrolyte is traditionally described as capacitor in parallel with a resistor, and pure electrical elements like capacitors and resistors are used for modeling the system. Moreover electrodes with rough surface areas have been reported to have high effective surface area, i.e. low impedance and high charge capacity. When a metal is introduced into solution containing its ions, the charge transfer takes place by charging/discharging of interfacial double charge layer or by reversible faradic reactions. For simplicity let us assume interface is capacitor as shown in Figure 5.5.

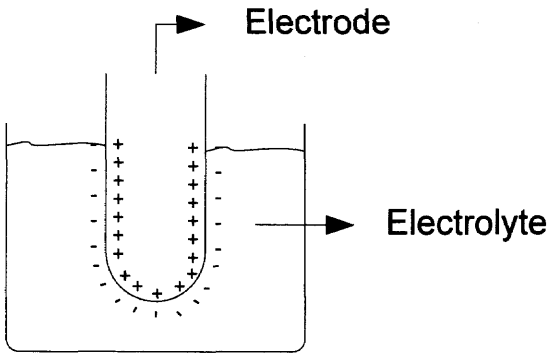

Figure 5.5 Approximate model of an interface as a simple capacitor.

The capacitance of a parallel plate capacitor is given by $C = \varepsilon A/d$. where A is the effective surface area of the plates, d is the distance between the plates and ε is dielectric constant of free space. In case of electrode-electrolyte interface the distance d is in the order of molecular radius hence resulting in high values of capacitance. But as the size of the electrodes reaching in the order micro scale, the parameter area (A) is not significantly explored to meet the requirements of present day neural prosthesis.

For a given surface, surface area can be defined in two ways:- *(Normal) Surface Area* is the area that is usually shown and dimensioned on a drawing. The normal surface area does not indicate anything about the surface and its roughness profile of the surface.

Projected Surface Area (Real Surface Area) is the actual surface area that depends on the properties, structure, material etc. of the object. The Real surface area can be many times larger than the Normal surface area. A ratio between the difference in the projected surface area and the normal surface area over the normal surface area can be used as a significant parameter to claim for the improvement in surface roughness.

For many applications roughness is analogous to surface finish and is used to claim certain parameters like friction. Similarly for stimulating/recording electrodes in neural

prosthesis, improvement in roughness of the electrode surface can be used intuitively, to claim an improvement in the charge injection capacities of the electrodes.

Electrodes with rough surface areas have been reported to have high effective surface area, i.e. low impedance and high charge capacity. Studies conducted on Pt, Ti and TiN coated electrodes by Norlin et al. supported this fact. Figure 5.6 shows SEM pictures of Pt, Ti and TiN coated with different degree of roughness used by Norlin et al.

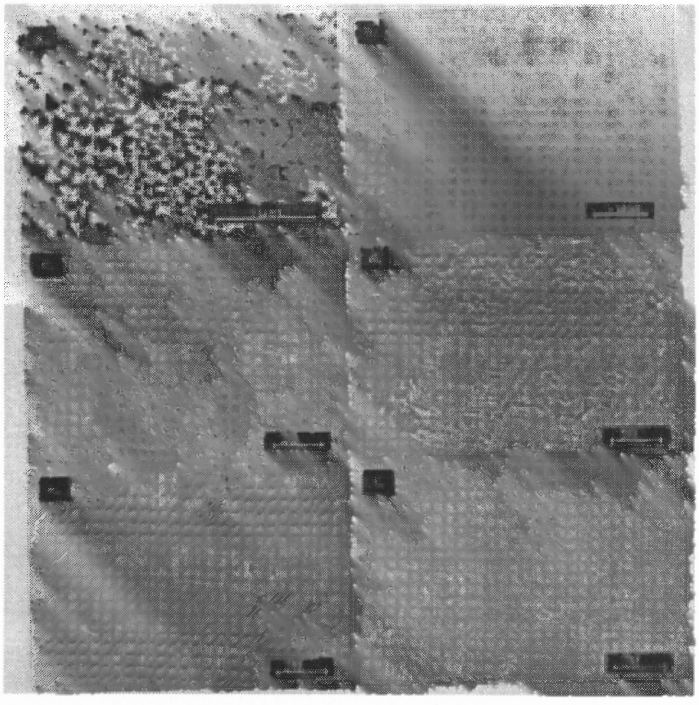

Figure 5.6 SEM picture of (a) Rough TiN (b) cross section of rough TiN (c) smooth Ti (d) smooth TiN (e) smooth Ti after 1000 cyc at 1.7V/s (f) smooth TiN after 1000 cycles at 1.7V/s [48].

Table 5.2 Numeric Values of Capacitance. Range of the Minimum of Three Measurements

Surface roughness	C (F/cm^2)
Smooth Pt	$4.3\text{-}5.7 \times 10^{-5}$
Smooth Ti	$1.6\text{-}1.7 \times 10^{-5}$
Smooth TiN on Ti	$4.7\text{-}5.5 \times 10^{-5}$
Rough TiN	$1.8\text{-}2.2 \times 10^{-2}$

Table 5.2 compares these surfaces with respective to electrode capacitance. As seen from the table 'Rough TiN' has approximately thousand times improvement in capacitance in comparison with the least numerical value of capacitance in the group (smooth Ti). Capacitance values for Smooth Pt and Smooth TiN on Ti are of same magnitude.

5.2 Reactive Ion Etch

Reactive Ion Etch (RIE) is a non-conventional technique used for nonuniform eroding of metal coating on the substrate to attain rough surfaces for specific applications. Wafer is mounted on a electrode which is grounded and RF power is applied to another electrode which is parallel to grounded electrode, a gas containing reactive species is flowed over the wafer. Later this gas is exited into plasma using RF power which will create highly reactive chemical species in close proximity to the wafer. The phenomena occurring during RIE can be grouped into two: *Chemical part of RIE*: In this reactive species accelerate towards, react at the surface of the material to be etched, forming gaseous byproduct. *Physical part of RIE*: Ions hitting the surface to be etched, transfer enough energy to the surface atoms, that some of the surface atoms get sputtered (knock out) without any chemical reaction. A typical parallel plate RIE reactor is as shown in Figure 5.7

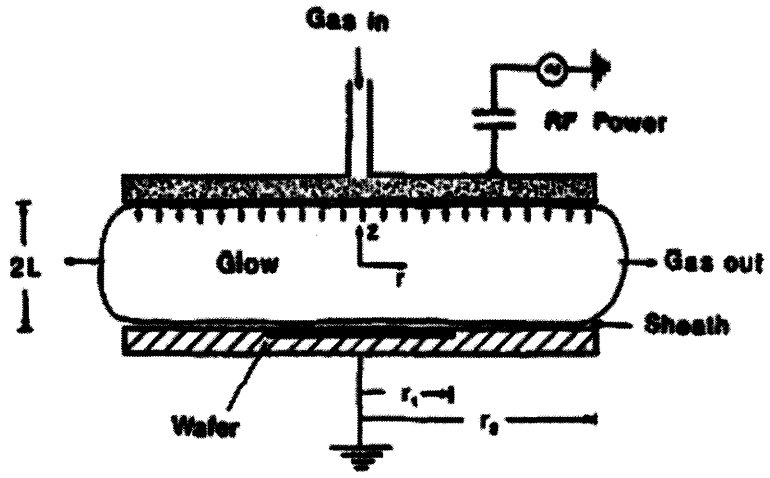

Figure 5.7 Schematic of a typical parallel plate plasma reactor [49].

Ability to delivery controlled power in a plasma discharge is of most importance in plasma assisted technologies like etching; usually predetermined radio frequency power required for the optimal use of the system is obtained by using a matching network between a radio frequency power source and the plasma discharge chamber electrodes or coupling coil. The matching network transforms the impedance (capacitive reactance) of the plasma discharge into a substantially resistive load for the radio frequency power source. The power source is then set to a predetermined power level dependant upon the process parameters desired.

The matching network between the radio frequency power source and plasma chamber electrodes consists of variable capacitors and/or inductors as the matching components. The matching network may be adjusted manually or automatically. This matching can be disturbed frequently to shut on and off the plasma in the reacting chamber, this is popularly termed as flickering technique and is used for non-uniform etching.

5.3 Platinization

Platinization is a method of depositing platinum in the solution on to an object to be coated. The essential components for platinization are the electrode or substrate to be coated, a secondary electrode to complete the circuit and an electrolyte containing platinum ions. The object to be platinized is connected to the negative terminal of a direct current source and the positive terminal of the current source is connected to a secondary electrode as shown in Figure 5.8. As the current is increased from zero, a point is reached where metal plating begins to occur. The current flowing through the solution ionizes it into positive and negative ions; metallic ions of the solution carry positive charge and are attracted towards negatively biased object to be coated and get deposited eventually.

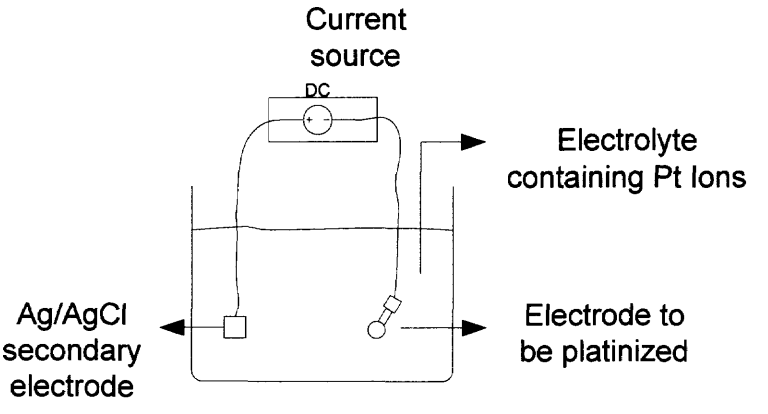

Figure 5.8 A basic platinizing electrochemical cell.

Essentially following reactions occurs at the electrodes:

cathode: $Pt^{2+}(aq) + 2\ e^{-} \Leftrightarrow Pt(s)$

anode: $Pt(s) \Leftrightarrow Pt^{2+}(aq) + 2\ e$

Here valance of platinum is shown as 2, in reality platinum can exits in 1,2,3,4 valance states. The electrons need for reduction of Pt onto the cathode is provided by the negative side of the current source and electrons released by oxidation of Pt in the solution are drained by positive of the current source.

Almost all metals can be coated with platinum. But the rate of deposition is determined by factors like amount of current, surface preparation, temperature, concentration of the electrolyte, bath stability etc. Rate of deposition of Pt can be optimized at room temperature by appropriately selecting other parameters.

5.4 Experimental

5.4.1 Reactive Ion Etch

A p-type single side oxide coated <100> silicon wafer was patterned using a mask, which had circular features with a diameter of 1mm each. Wafer was spin coated first with primer at 800 rpm for 1 minute, later with photo resist for a thickness 1.5μ (approximately) at 1000 rpm for 1 minute. Followed by UV exposure, developing, inspection and hard baking (details of each step is discussed in chapter 2)

Sputtering of Titanium (Ti) was done using Varian DC 3125 PVD system for a thickness of 900nm. Then the wafer was put in acetone bath for lift off of excess of Ti. Finally the wafer was cut into pieces; each sample having at least two of the circular features. These cut samples were etched separately using either CF4 or SF6 along with O_2 at different power, gas pressure and amounts of reactants in Minilock Reactive Ion Etch system. Impedance matching between RF generator and Plasma was manually altered between match

and mismatched states; due to this plasma inside the chamber was flickering on and off, this technique is reported to enhance non uniform etching of the surface.

Later charge injection capacity (CIC) for each piece was measured in phosphate buffered saline (PBS) solution using biphasic symmetric current pulse, LabView program was used to control pulse width to 0.5 ms. The circuit used for these stimulations is shown in Figure 5.9 Potentiometer 1 in the circuit is to control the strength of stimulating current within the water window of electrode assumed to be 1V and potentiometer 2 is used to set the bias voltage to -0.5 V.

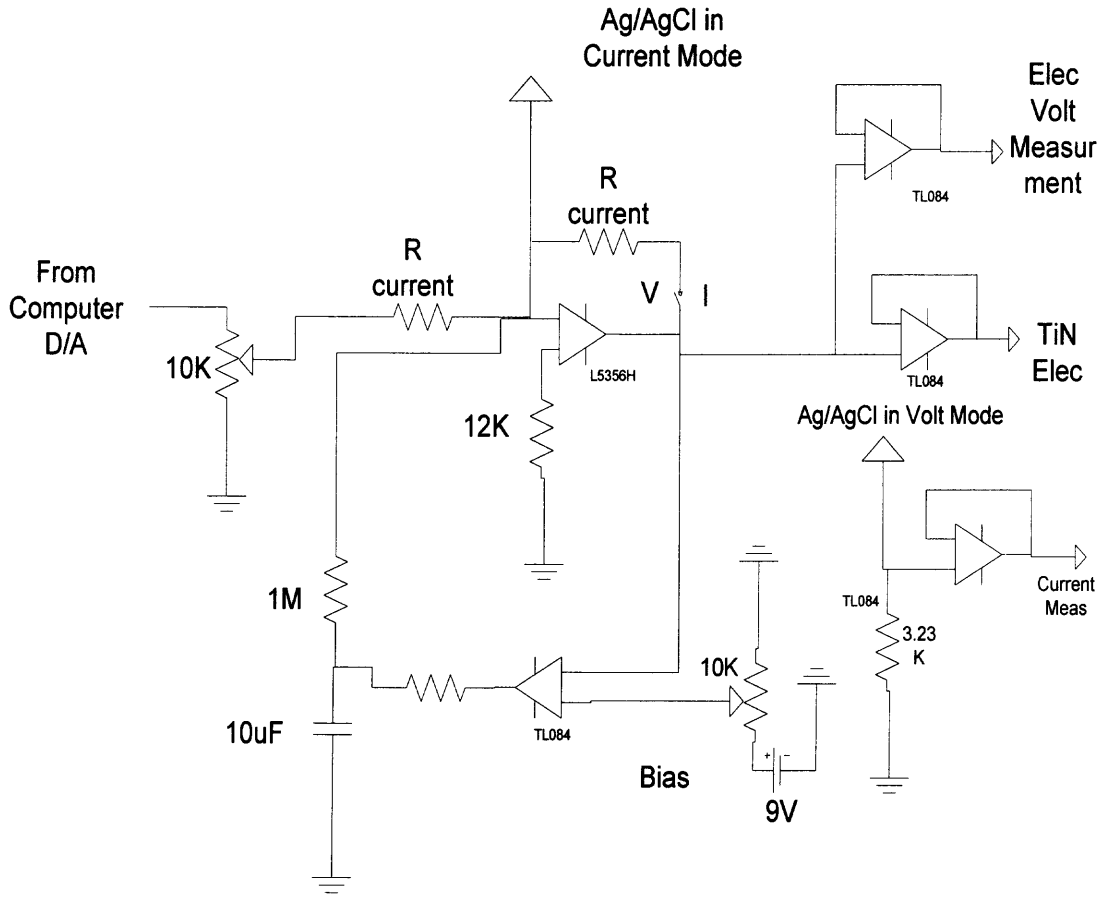

Figure 5.9 Custom designed circuit for charge injection capacity measurements.

The Table 5.3 gives details how each sample was treated in the RIE chamber. Samples 1 and 2 are not treated, samples 3 was treated CF_4 but with no flickering, sample 4 was treated with SF6 and with flickering, samples 5, 6, 7 are treated with CF_4 and with flickering.

Table 5.3 Sample Treatment in RIE Chamber and their Respective CIC

Sample No.	Treatment Gas CF_4/SF_6	Pressure (mtorr)	RF Power (Watt)	Flickering	Time (Sec)	CIC($\mu C/cm^2$)
1.	Untreated	-	-	-	-	22.2
2.	Untreated	-	-	-	-	25.4
3.	CF_4 10cc	100	200	NO	180	32.6
4.	SF_6 50 cc	300	150	YES	40	22.3
5.	CF_4 50 cc	300	250	YES	60	24.4
6.	CF_4 10 cc	80	200	YES	120	60.4
7.	CF_4 50 cc	150	250	YES	180	65.2

Here Table 5.3 gives details how each sample was treated in the RIE chamber and corresponding CIC. Samples 1 and 2 are not treated, but cleaned with IPA and distilled water before CIC measurements, samples 3 was treated CF_4 but with no flickering, sample 4 was treated with SF_6 and with flickering, samples 5,6,7 are treated with CF_4 and with flickering.

Sample 4 treated with 50cc SF_6, at 150 Watt, at 300mtorr of gas pressure for 40 sec and with flickering has the least CIC (22.3mc/cm^2), Followed by the untreated samples 1&2 (22.2 mc/cm^2 and 25.4mc/cm^2), then samples 3 treated with 10cc CF_4, at 200 Watt, at 100mtorr of gas pressure for 180 sec and with NO flickering (32.6mc/cm^2). Samples 6&7 treated CF_4 at different pressures and power for longer time (120 sec and 180 sec) has approximately three times improvement in the CIC as compared with untreated ones. A sample 5 treated with CF_4, at 250watt; at 300mtorr for 40 sec don't show significant improvement in the CIC as similarly treated samples for longer time.

5.4.2 Platinization of Titanium

Platinization of Titanium electrodes was done using 0.0035 M platonic acid + 0.01M HCl purchased from Sigma Aldrich. Platonic acid (H_2PtCl_6) obtained from Sigma Aldrich was 0.019521M, 8% by weight solution and molecular weight of anhydrous H_2PtCl_6 was 409.81g. Required molarity of 0.0035M was obtained by adding 4.5ml of distilled water to 1ml of H_2PtCl_6.

Molarity: molarity of the solution is defined as amount of moles present in one liter of solution.

Molarity of H_2PtCl_6 = 8/409.8
= 0.019521M (moles/liter)
Required molarity = 0.0035M

Amount of dilution = 0.019521/0.0035
= 5.5 times

Meaning 1ml of H_2PtCl_6 should be made 5.5 ml to obtain required molarity.

Similarly HCl purchased from Sigma Aldrich was 1N, a molarity of 0.01M was obtained by diluting 1ml of 1N HCl by 100 times, using distilled water.

(Molarity (M) = Normality (N) for HCl because, for HCl molecular weight equal to atomic weight).

For a Charge = 10 C/cm^2 and current of 1μA. time required for platinizing a typical electrode was calculated as follows.

Charge = 10 C/cm^2
Current = 1μA => 1μA/A (5026$\mu m^{2)}$ = 1.99×10^4 μA/ cm^2

where A is area of electrode
Time = 10 C/cm^2 / 1.99×10^4 $^{\mu}A/ cm^2$
= 502.51 sec.

CIC measurements were made in PBS using symmetric, bi-phasic current pulse, with bias voltage of -0.5V and with pulse width of 0.5ms. Current amplitude was limited to water window of stimulating electrode as 1V. The results in Table 5.3 shows maximum CIC values obtained after platinization of Ti. Circuit for these recordings is shown in Figure 5.9.

Table 5.4 CIC of Platinized Platinum

	CIC (mC/cm^2)	Contact Area (μm^2)	Geometry square / circular
Contact 1	2	6400	square
Contact 2	2.1	6400	square
Contact 3	2.3	5026	circular
Contact 4	2.9	5026	circular

Here Table 5.4 shows CIC measurements of four samples after platinization. Contacts 1 and 2 are square and Contacts 3 and 4 are circular.

Fixing the charge and amount of current for platinization; Square (6400μm^2) contacts are platinized for 16 minutes and circular (area=5026μm^2) contacts were platinized for 9 minutes. The average CIC is 2.3 (mC/cm^2).

5.4.3 Dependency of Charge Injection Capacity on Electrode Size

Model's of electrode-electrolyte interface shows that current-voltage characteristics of the electrodes-electrolyte interface are non-linear, so a need to use a non-linear element. Furthermore, the half-cell potential of the electrode is considered as a double-layer of charge appearing on the surface of the electrode. Two layers of charge of opposite sign, separated by distance, is simply a capacitor. Modeling of this interface helps in predicting its behavior using different kinds of conditions, like using different amplitudes of input voltages, different bias voltages, or different contact area sizes. But, measurements involving mere particle elements are showing evidence that these elements are not enough for modeling the interface, particularly as the electrode size goes in the order of micro meters. As the electrode size becomes smaller, a question that needs to be answered is how the electrode electrolyte interface properties effect the current and voltage measurements near the electrode surface and do these measurements scale down for electrodes with very small surface area.

Maximum injectable charge and double charge layer capacitance values were reported for titanium nitride (TiN) electrodes before however, only for a selected contact size. In this experiment we measured the charge injection capacity (CIC) of titanium

nitride electrodes with three different surface areas for comparison. The pulse method was used for the measurements.

Titanium electrodes of three different sizes (177μm^2, 1250 $\mu m^2$and 4000μm^2) fabrication of those electrodes is discussed previously, the electrodes were placed in a phosphate buffer saline (pH=7.4) and a charge balanced cathodic first biphasic current stimulus pulse was applied. Both cathodic and anodic phase were either 0.2ms or 0.5ms long with a 0.02ms break in between. The current stimulator was custom designed to ensure a fast rise time (<0.5μs). The back voltage from electrode was first buffered with a unity gain amplifier (TL084, Texas inst) and sampled into a computer using a data acquisition board (PCI 6071) and LabView software (Both from National Inst.) at a sampling rate of 1.25Mhz.

The current pulse amplitude was increased incrementally until the double charge layer voltage reached-1.0 Volts Figure 5.10 shoes the voltage waveform for a pulse duration of 0.5ms at a current amplitude of 100μA measured with different surface area electrode(177μm^2,1250 $\mu m^2$and 4000μm^2). The instantaneous jump in the voltage at the onset of the current pulse is due to the access resistance and the resistance of interconnects. This initial voltage step is subtracted from the peak voltage for calculation of the double charge layer voltage that develops during the cathodic phase of the current pulse.

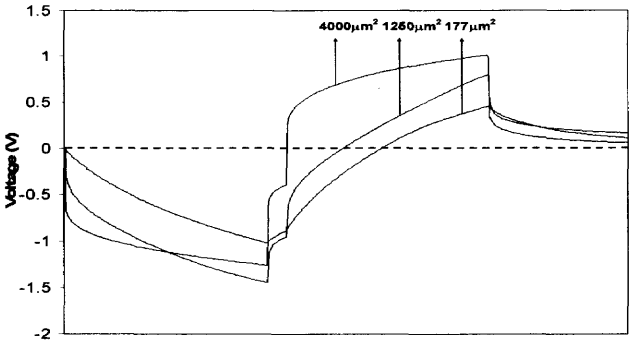

Figure 5.10 Voltage across the current sink in response to a current pulse, measured with surface area 177μm^2, 1250 μm^{2}and 4000μm^2.

The mean and standard deviation for the normalized CIC measured for all electrodes sizes at both pulse durations (0.2ms and 0.5ms) are shown in Table 5.5. The total number of electrodes for each kind are shown as n. The table shows that the total CIC for unit area of the electrode is increasing with the electrode size.

Table 5.5 Mean and SD of CIC for Different Electrode Sizes

	Mean ± SD (177μm^2)	Mean ± SD (1250μm^2)	Mean ± SD (4000μm^2)
Qinj2 (mC/cm^2)	0.25 ± 0.06 (n=13)	0.49 ± 0.06 (n=9)	0.80 ± 0.06 (n=6)
Qinj5 (mC/cm^2)	0.36 ± 1.0 (n=13)	0.88 ± 1.0 (n=9)	1.41 ± 1.0 (n=6)
Cp2(μF/cm^2)	0.27 ± 0.08 (n=13)	5.92 ± 0.08 (n=9)	32.34 ± 0.08 (n=6)
Cp2(μF/cm^2)	0.40 ± 0.13 (n=13)	10.08 ± 0.13 (n=9)	58.43 ± 0.13 (n=6)

5.4.4 Charge Injection Capacity and Bias Voltage

The electrodes were placed in a phosphate buffered normal saline (pH=7.4) at room temperature and the bias voltage was adjusted with a custom-built circuit with respect to a large Ag/AgCl reference electrode. A charge balanced, cathodic first, biphasic current stimulus pulse train was applied at 50Hz. Both cathodic and anodic phases were 0.5ms long and of the same amplitude. The current stimulator was custom designed to ensure a fast rise time (<0.5μs) and thereby allowing an accurate measurement of the access voltage at the onset of the current pulse. The back voltage from the electrode was fist buffered with a unity gain FET amplifier before sampled into a computer using data acquisition board (PCI 6071) and LabVIEW software (both from National Inst.) at a sampling rate of 1MHz. Spike triggered averaging method was employed to remove the noise from the signals.

The bias voltage was varied between -0.9V and -1.5V in steps of 0.1V and the current amplitude was determined that generated an excursion of -1.0V in the electrode back voltage. The initial voltage jump at the onset of each current pulse that was due to the access resistance was subtracted in calculation of the back voltage. As a comparison, the charge injection limit for a voltage excursion of -2.0V was also determined since there was still no evidence of bubble generation at this potential. Fifteen contacts of size 177μm^2, 12 contacts of size 1250μm^2, and 9 contacts of size 4000μm^2 were studied.

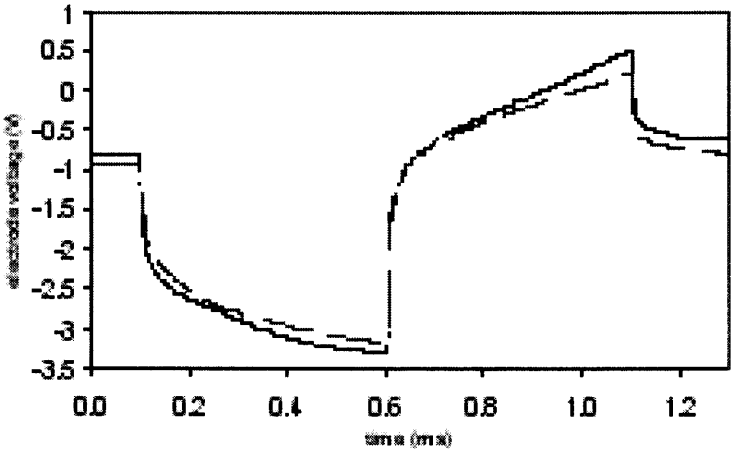

Figure 5.11 Back voltage of a TiN electrode as a response to current pulses of 18μA (solid line) and 15μA (dash line) amplitude and a pulse duration of 0.5ms. The plateau at the end of the cathodic phase around -3.3V suggests H_2 evolution in the first plot. The second plot at a lower current seems free from any distortion. The electrode area is 177μm^2 and the bias voltage is -1.0V. The initial jump due to the access resistance was measured as 0.2V within the first 2μs.

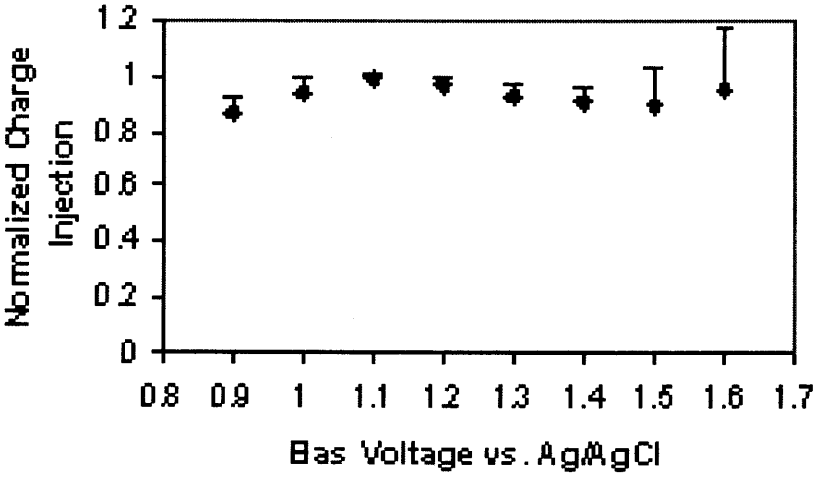

Figure 5.12 Charge injection capacity as a function of the bias voltage measured from TiN contacts of 177μm^2 size (n=15). The measurements from each contact were normalized with respect to the maximum charge within the bias voltage range of -1.0 to -1.4V. Standard deviations are shown as vertical bars. The mean value of the charge without normalization was 1.68±0.24mc/cm^2 for the bias voltage of -1.1V.

Figure 5.12 shows the electrode voltage with one of the 177μm^2 size contacts for a bias potential of -1.0V where the current amplitude was increased until the H_2 evolution

was evident with a plateau at the end of the cathodic cycle. The voltage step due to the access resistance was about -0.2V (measured within the first 2μs) and the plateau occurs around -3.3V. In Figure 5.11, the electrode voltage is also shown when the peak-to-peak electrode voltage was limited at -2.0V (-3.2V peak). Neither the anodic nor the cathodic cycle exhibits any distortion suggesting a chemical reaction. The total injected charge in this case was 4.24mC/cm^2.

The charge injection limit measured for a range of bias voltages are normalized and plotted in Figure 5.12 for the 177μm^2 contacts studied. The mean value of the injectable charge is maximum for the bias voltages between -1.0V and -1.3V. Without normalization, the maximum injectable charge was 1.68±0.24mc/cm^2 (n=15) at the holding potential of -1.1V. A small increase at the higher end is observed because of possible hydrogen evolution, which allows the passage of larger currents without an increase in the back voltage and thereby fictitiously inflating the measure of total charge injected.

The electrodes with larger areas did not show a clear peak in the charge vs. bias voltage plot. The injectable charge was 2.1±0.37mc/cm^2 (n=12) and 1.98±0.37mc/cm^2 (n=9) at the bias voltage of -1.1V for the 1250μm^2 and 4000μm^2 contacts respectively.

Similar measurements made with NJIT patterned electrodes with surface area 5026μm^2, for three different bias voltages showed dependency of injectable charge on bias voltage. Maximum charge was 1.9 mc/cm^2 ± 0.8 (n=4) for a bias voltage of -1.2V.

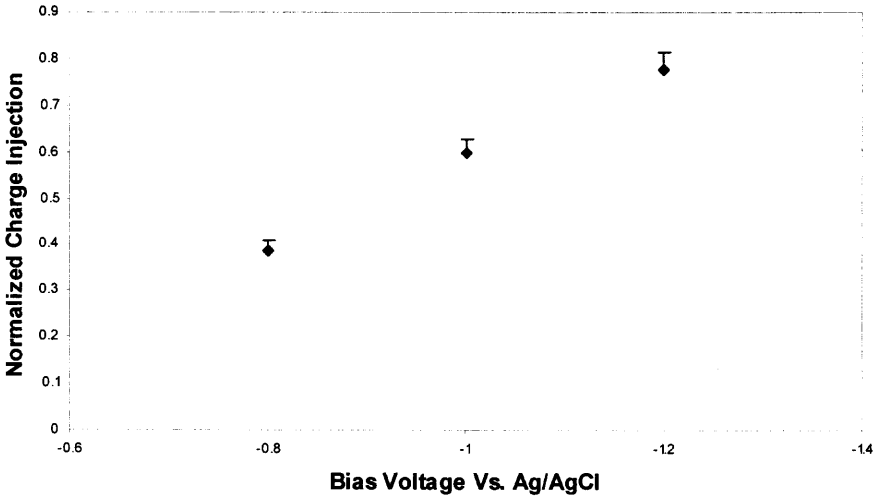

Figure 5.13 Charge injection capacity as a function of the bias voltage measured from TiN contacts of 5026μm^2 size (n=4) for NJIT patterned electrodes.

5.4.5 Charge Injection Capacity for Extended Voltage Range

Several groups reported on maximum injectable charge of TiN electrodes within the voltage window of the water electrolysis as -1.0V Recently, another group studied TiN electrodes with rough surfaces using voltammetry in the voltage range of -3.0V to 1.0V and found that the CV plot became linear and independent of the sweep rate at fast sweeping rates (>10V/s). The charge-transfer process was "almost completely reversible" for this voltage range and no evidence of bubble generation was observed.

If it is proven to be safe, an extended voltage limit into the cathodic cycle can increase the charge injection capacity of TiN electrodes significantly for neural stimulation. Therefore, in this experiment, we investigated the maximum injectable charge with TiN electrodes using current pulses for an extended cathodic voltage range. Also a dependency CIC on electrode voltage and bias voltage was investigated.

The electrodes were placed in a phosphate buffered normal saline (ph=7.4) at room temperature and the bias voltage was controlled with a custom-built circuit with respect to a large Ag/AgCl reference electrode. A charge balanced, cathodic first, biphasic current stimulus pulse train was applied at 50Hz. Both cathodic and anodic phases were 0.5ms long and of the same amplitude. The current stimulator was custom designed to ensure a fast rise time (<0.5μs) and thereby allowing an accurate measurement of the access voltage at the onset of the current pulse. The back voltage from the electrode was first buffered with a unity gain FET amplifier before sampled into a computer using data acquisition board (PCI 6071) and LabVIEW software (both from National Inst.) at a sampling rate of 1MHz. Spike triggered averaging method was employed to remove the noise from the signals.

The bias voltage was set within the range of -0.8V to -1.4V (as studies in section 5.4.4 gave maximum inject able charge for the bias voltages between -1.0V and -1.3V) and the current amplitudes were determined that generated a range of electrode back voltages from the bias voltage down to -3.0V in steps of -0.2V. The initial voltage jump due to the access resistance was subtracted in calculation of the back voltage. Six TiN contacts with an area of 177μm^2 were studied.

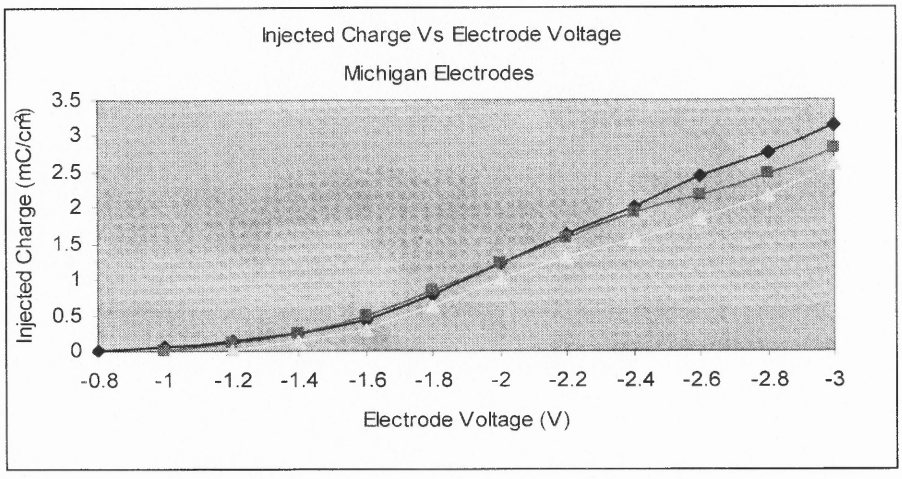

Figure 5.14 Injected charge as function of the electrode voltage for three different bias voltages: -1.2(▲), -1.0(■), and -0.8V (♦) measured with Michigan electrodes.

The injected charge is shown in Figure 5.14 as a function of the electrode peak voltage in the cathodic phase for three different values of the bias voltage (-0.8V, -1.0v and -1.2V). The charge increases first slowly and then at a higher rate beyond the electrode voltage of -1.6V in all three cases. The maximum inject able charge is 4.45mC/cm^2 for a bias voltage of -0.8V.

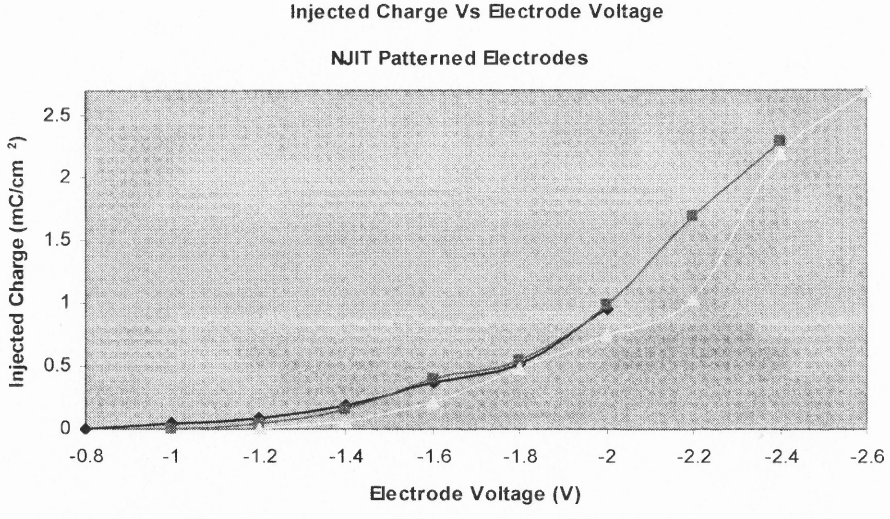

Figure 5.15 Injected charge as function of the electrode voltage for three different bias voltages:-1.2(▲), -1.0(■), and -0.8V (♦) measured with NJIT patterned electrodes.

The Figure 5.15 shows mean charge injection capacity of seven electrodes plotted against electrode peak voltage in the cathodic phase with bias voltages voltage (-0.8V, -1.0V and -1.2V), as seen in Michigan electrodes, the injected charge increases slowly at first and then rapidly beyond -2V. Maximum charge injection capacity for these electrodes is 2.6mC/cm^2 for a bias voltage of -1.2V.

5.4.6 Charge Injection Capacity Comparison

One of the objectives of this study was to study the charge injection capacity of NJIT patterned electrodes in comparison with Michigan reference electrodes.

Table 5.6 shows the measurements made on six electrode (1-7853μm^2, 2-10000μm^2 and 3-5026μm^2) at three different bias voltages (-0.8V, -1.0V and -1.2V).

Table 5.6 Measurements Made with NJIT Patterned Electrodes

Contact:1 Area:(μm²)	Bias: -0.8V 7853.9			Bias: -1V			Bias:-1.2V		
		I (μA)	CIC		I (μA)	CIC		I (μA)	CIC
	1	3	0.019099						
	1.2	7	0.044564	1.2	6	0.038198			
	1.4	24	0.15279	1.4	22	0.140058	1.4	6	0.038198
	1.6	60	0.381976	1.6	64	0.407441	1.6	20	0.127325
	1.8								
	2								
Conatct:2 Area:(μm²)									
	10000								
	1	6	0.03						
	1.2	22	0.11	1.2	14	0.07			
	1.4	64	0.32	1.4	38	0.19	1.4	28	0.14
	1.6			1.6	220	1.1	1.6	120	0.6
	1.8			1.8					
	2								
Contact:3 Area:(μm²)	10000								
	1	12	0.06						
	1.2	32	0.16	1.2	20	0.1	1.4	24	0.12
	1.4	72	0.36	1.4	52	0.26	1.6	110	0.55
	1.6	180	0.9	1.6			1.8	200	1
	1.8			1.8					
	2								
Contact:1 Area:(μm²)	5026								
	1	3	0.029845						
	1.2	5	0.049741	1.2	5	0.011938			
	1.4	14	0.139276	1.4	12	0.119379	1.4	5	0.049741
	1.6	24	0.238758	1.6	24	0.238758	1.6	10	0.099483
	1.8	80	0.795862	1.8	38	0.378034	1.8	15	0.149224
	2	120	1.193792	2	100	0.994827	2	30	0.298448
							2.4	52	0.51731
Conatct:2 Area:(μm²)	5026								
	1								
	1.2			1.2		0.011938	1.4		
	1.4	7.5	0.074612	1.4	7.5	0.074612	1.6	6	0.05969
	1.6	12	0.119379	1.6	14	0.139276	1.8	17.5	0.174095
	1.8	36	0.358138	1.8	40	0.397931	2	52	0.51731
	2	80	0.795862	2	56	0.557103	2.4	60	0.596896
Contact:3 Area:(μm²)	5026								
	1	5	0.049741						
	1.2	8	0.079586	1.2	4	0.011938			
	1.4	14	0.139276	1.4	8	0.079586	1.4	2	0.019897
	1.6	40	0.397931	1.6	15	0.149224	1.6	10	0.099483
	1.8			1.8	60	0.596896	1.8	30	0.298448
				2					
Contact:4 Area:(μm²)	5026								
	1			1					
	1.2	6	0.05969	1.2	6	0.011938			
	1.4	12.5	0.124353	1.4	20	0.198965	1.4	7.5	0.074612
	1.6	20	0.198965	1.6	40	0.397931	1.6	32	0.318345
	1.8	40	0.397931	1.8	80	0.795862	1.8	80	0.795862
	2	88	0.875448	2	140	1.392758	2	140	1.392758
				2.2	170	1.691206	2.2	200	1.989654
				2.4	230	2.288102	2.4	220	2.188619
							2.6	270	2.686033

The electrodes were placed in a phosphate buffered normal saline (pH=7.4) at room temperature and the bias voltage was controlled with a custom-built circuit with respect to a large Ag/AgCl reference electrode. A charge balanced, cathodic first, biphasic current stimulus pulse train was applied at 50Hz. Both cathodic and anodic phases were 0.5ms long and of the same amplitude.

The bias voltage was set either -0.8V,-1V or -1.2V and the current amplitudes were determined that generated a range of electrode back voltages from the bias voltage down to -2.6V in steps of -0.2V. The initial voltage jump due to the access resistance was subtracted in calculation of the back voltage.

The maximum charge injection capacity for NJIT patterned electrodes was 2.68mC/cm^2 for bias voltage of -12V and The maximum charge injection capacity of Michigan electrodes was 4.45mC/cm^2 for a bias voltage of -0.8V.

APPENDIX

MASK USED FOR FABRICATION OF NJIT PATTERNED ELECTRODES

Mask1: Used for Patterning Titanium as First Layer

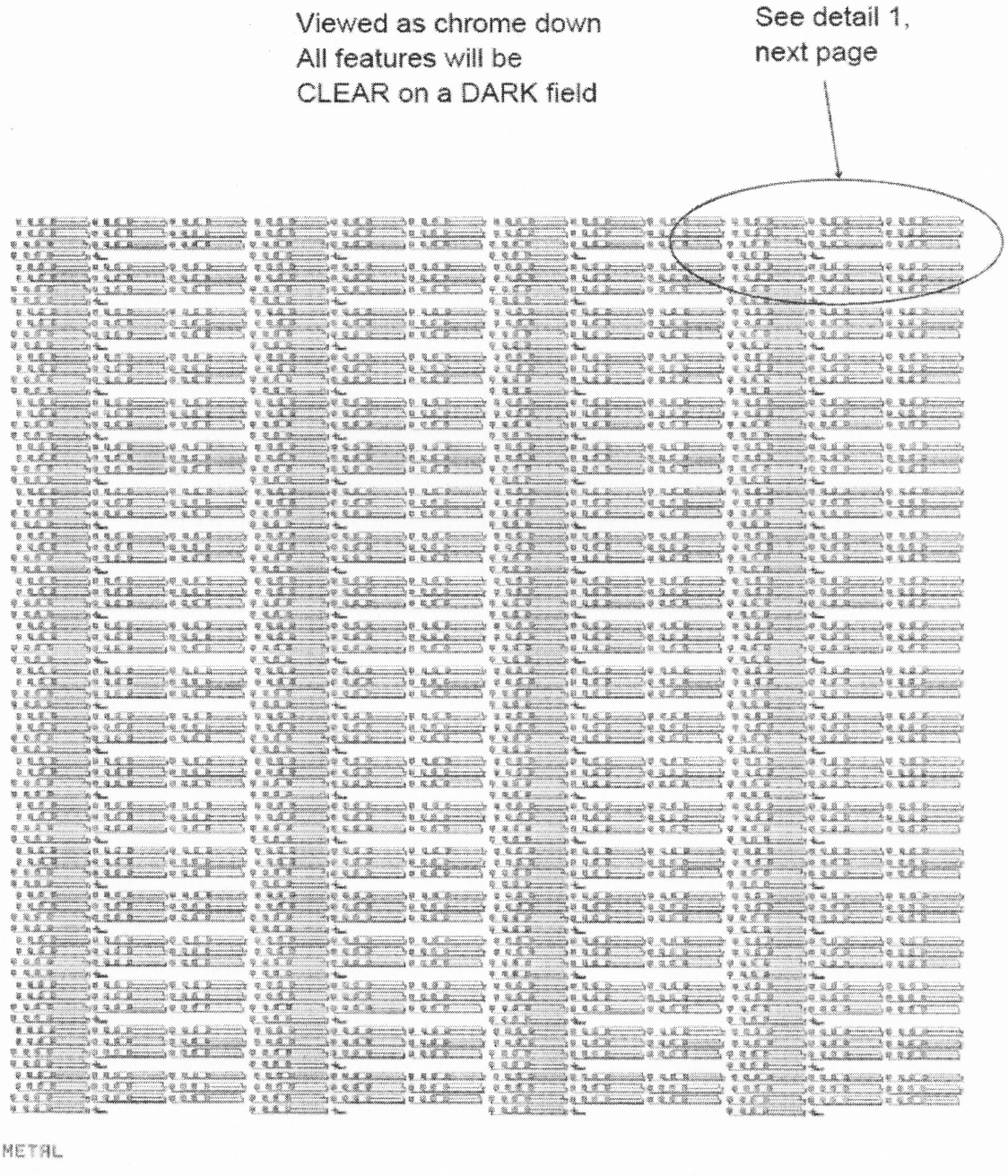

Mask1: Detailed View 1

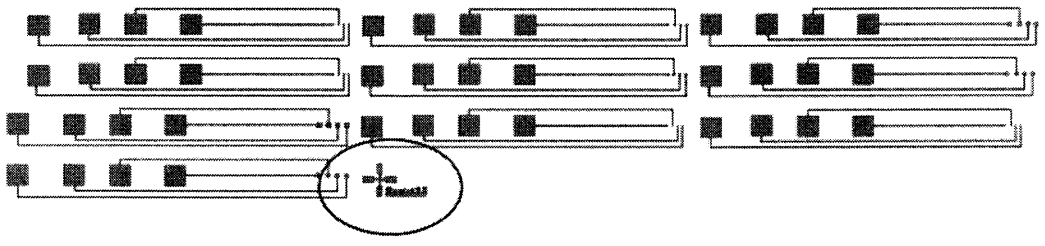

See detail 2

Mask1: Detailed View 2

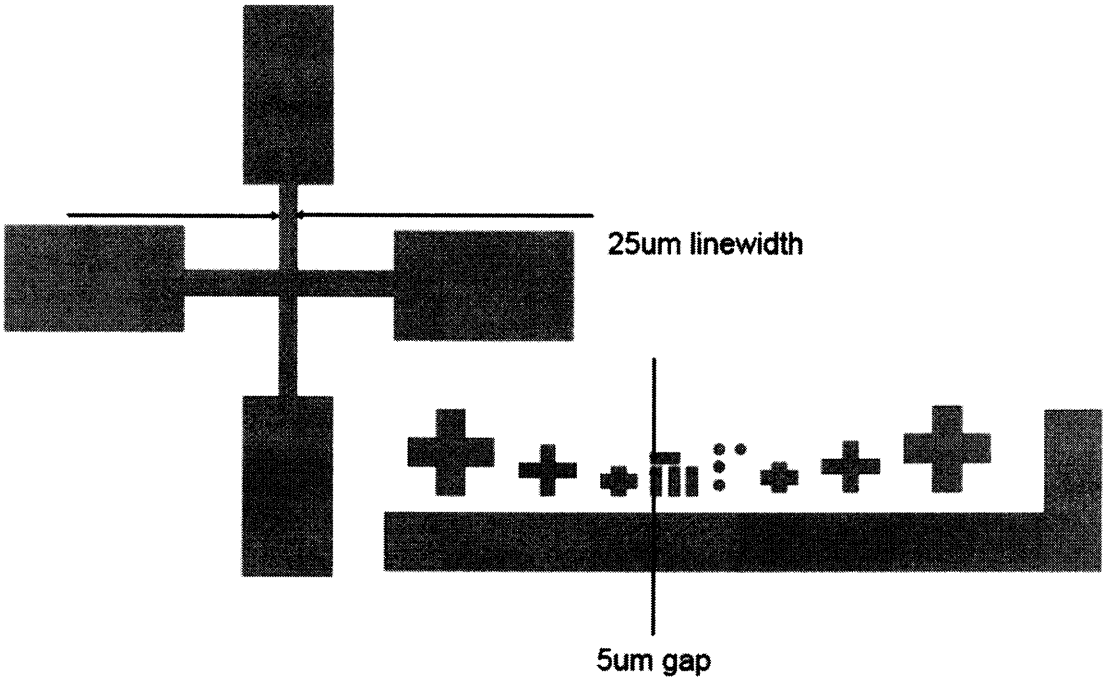

Mask 2: Used for Sputtering of Titanium Nitride on Electrodes

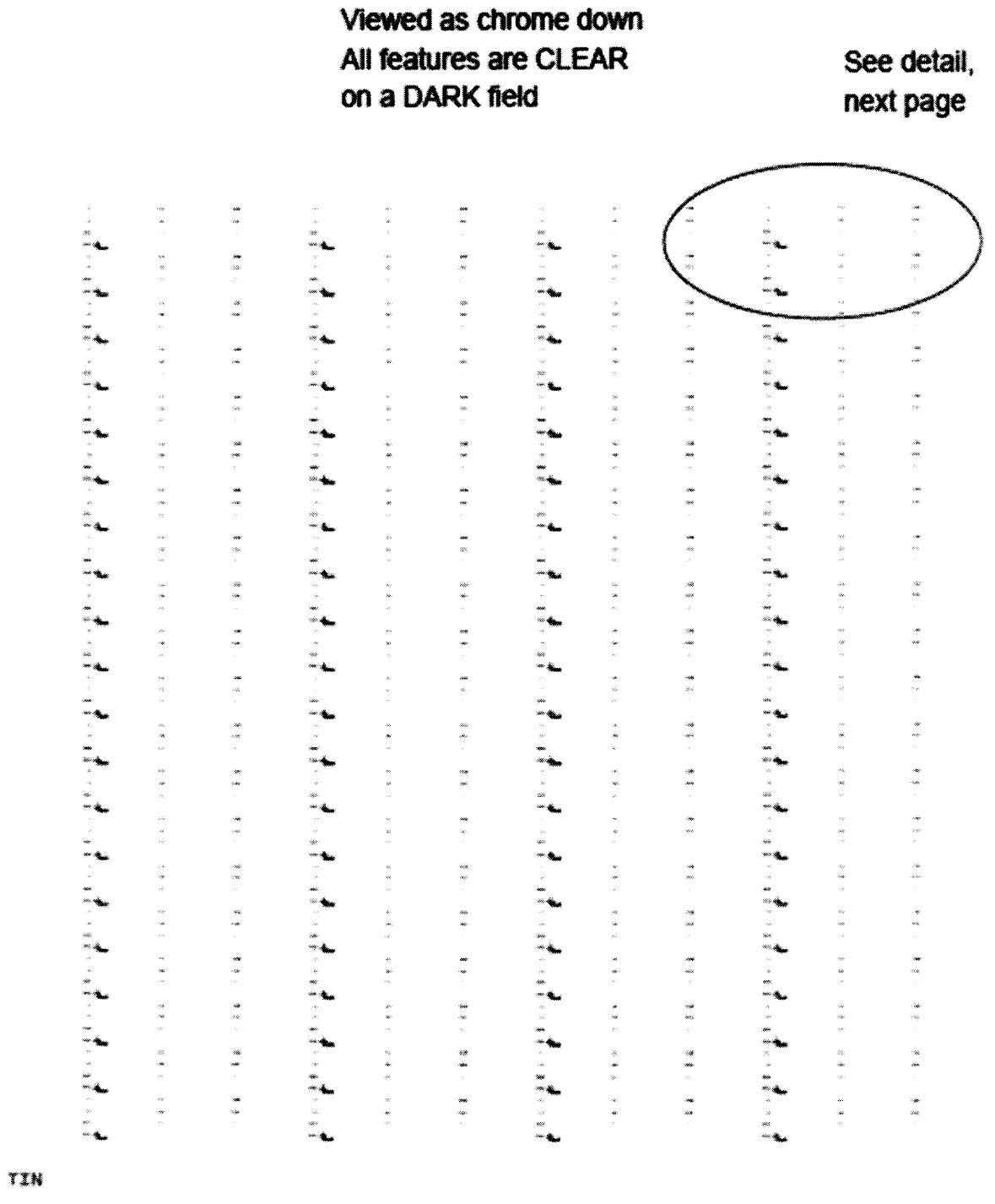

Mask 2: Detailed View

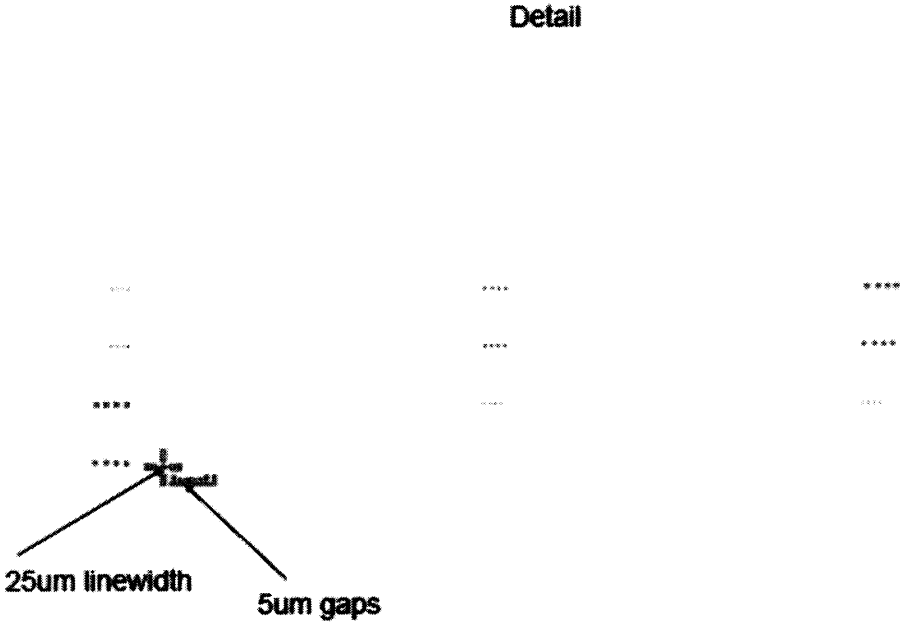

Mask 3: Used for Insulation of Titanium Metal Lines

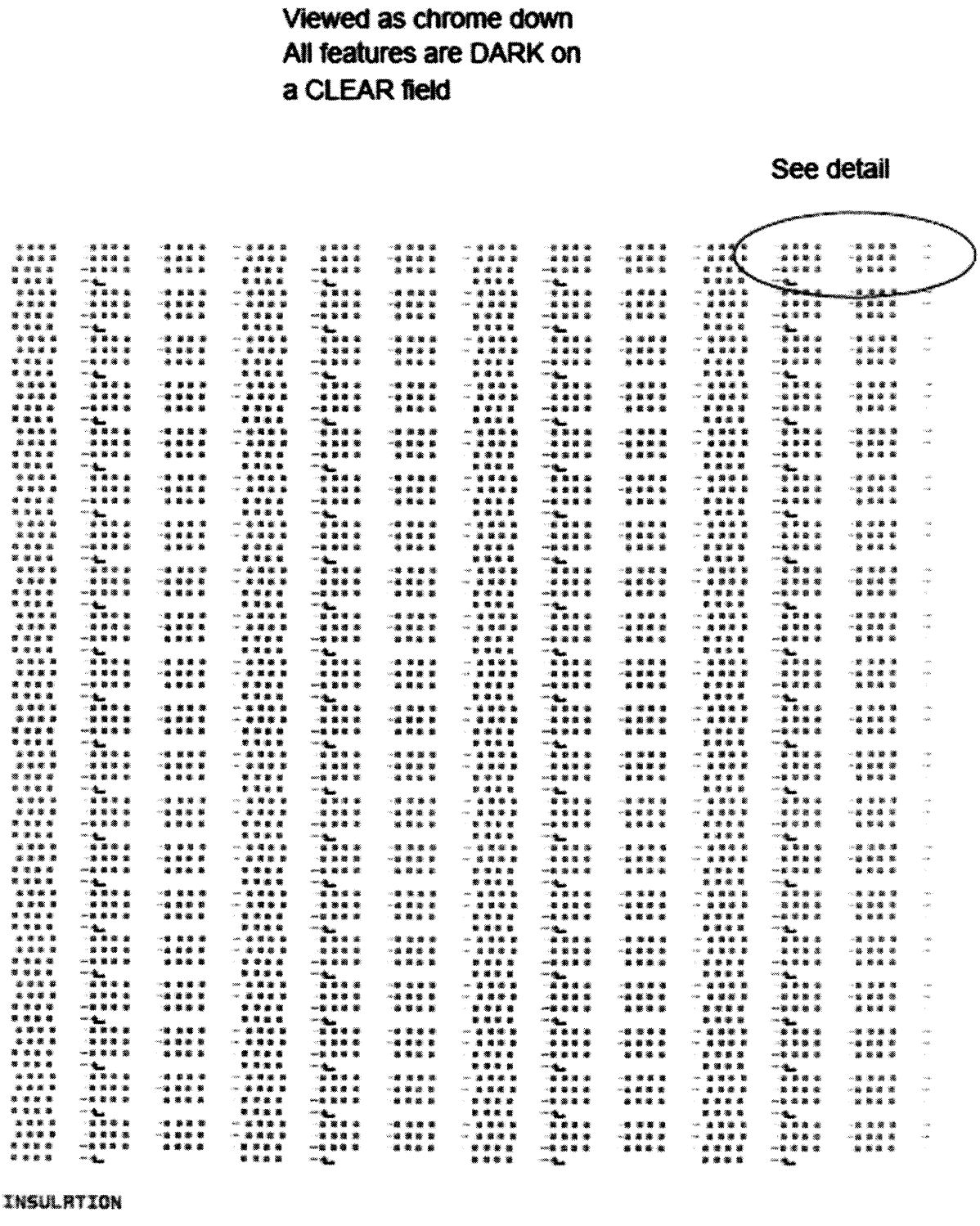

Mask 3: Detailed View

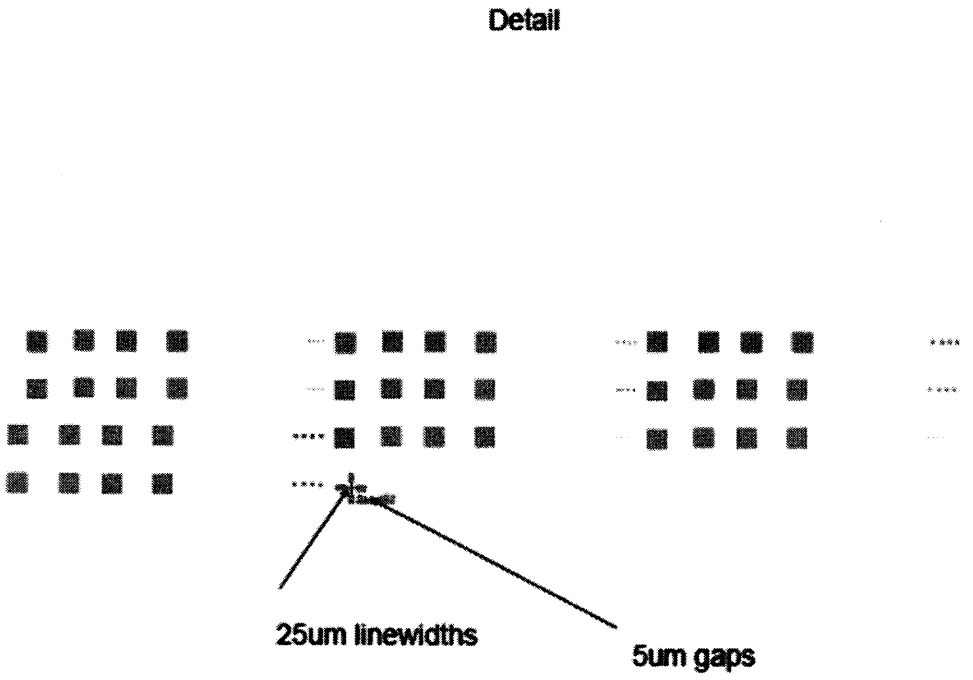

REFERENCES

1. G.W. Gross, B. Rhoades, and R. Jordan, "Neural Network for Biochemical Sensing", Sensors and Actuators, vol. 6, pp. 1-8, 1992.

2. R. Gaumond, J. Moyer, R. Silva, "A Whole-Cell Neurosensor: Simulation of Summed Asynchronous Neural Activity", Proceedings of the IEEE 28th annual northeast Bioengineering conference, pp.27 – 28, April 2002.

3. Website: www. wikimedia.org, November 11, 2006.

4. John G. Webster, "Medical Instrumentation: Applications and Design", Second Edition, 1978.

5. Jones. G. J, and D. M. Bollinger, "The Measurement of the Conductance of Electrolytes", Journal of Solution Chemistry, pp.280-284, 1935.

6. L. A. Geddes, C. P. Da Costa and G. Wise, "The Impedance of Stainless-Steel Electrodes", Journal of Medical and Biological Engineering and Computing vol. 9, pp 511-521, 1971.

7. L. A. Geddes, "How Measuring of Electric Current has Improved through the Ages", IEEE Potentials 15, pp.40-45, 1996.

8. S. B. Brummer, L. S. Robblee, and F. T. Hambrecht, "Criteria for Selecting Electrodes for Electrical Stimulation: Theoretical and Practical Considerations," Ann. N.Y. Acad. Sci., vol. 405, pp. 159–171, 1983.

9. D. B. McCrery, W. F. Agnew, T. G. H. Yuen, and L. Bullara, "Charge Density and Charge per Phase as Cofactors in Neural Injury Induced by Electrical Stimulation", IEEE Trans. Biomed. Eng., vol. 37, pp. 996–1001, Oct. 1990.

10. James D. Weiland, David J. Anderson, and Mark S. Humayun, "In Vitro Electrical Properties for Iridium Oxide Versus Titanium Nitride, Stimulating Electrodes" IEEE transactions on Biomedical Engineering, vol. 49, No. 12 December 2002.

11. S.B Brummer and M.J Turner, "Bioelectrochemistry and Bioengineering", pp. 2-13 1997.

12. S. B. Brummer and M. J. Turner, "Electrical Stimulation of the Nervous System: The Principle of Safe Charge Injection with Noble Metal Electrodes," Bioelectrochem. Bioeng., vol. 2, pp. 13–25, 1975.

13. A. Bolz, M. Hubmann, R. Had, J. Riedmuller, and M. Schaldach, "Low Polarization Pacing Lead for Detecting the Ventricular-Evoked Response", Medical Progress through Technology, vol. 199, pp. 129-137, 1993.

14. C. Moor, M Schmidt, A. Bolz, "Wireless Monitoring of Distributed Intelligent Medical Sensor Systems", IOS press, pp.137-139, 2004.

15. M. Janders, U. Egert, M. Stelzle, and W. Nisch, "Novel Thin Film Titanium Nitride Micro-Electrodes with Excellent Charge Transfer Capability for Cell Stimulation and Sensing Applications", 18th Annual International Conference of the IEEE Engineering in Medicine and Biology society, pp. 245-247, 1996.

16. Xiubo Tian, Langping Wang, Ricky King-Yu Fu and Paul K. Chu "Bias Voltage Influence on Surface Morphology of Titanium Nitride Synthesized by Dynamic Nitrogen and Titanium Plasma Immersion Ion Implantation and Deposition", Materials Science and Engineering journals, vol. 337, pp. 236-240, November 2002.

17. M. Schaldach, M. Hubmann, A. Weikl, and R. Hardl, "Sputterdeposited TiN Electrode Coatings for Superior Sensing and Pacing Performance", vol. 3, pp. 1891-1895, 1990.

18. X. B. Tian, Z. M. Zeng, B. Y. Tang, K. Y. Fu, D. T. K. Kwok and P. K. Chu "Properties of Titanium Nitride Fabricated on Stainless Steel by Plasma-Based Ion Implantation/Deposition", vol. 282, Issues 1-2, pp. 164-169, 30 April 2000.

19. A. Loinaz, M. Rinner, F. Alonso, J.I Onate, W. Ensinger, "Surface Coating Technology", pp.262, 1998.

20. S. Joseph Anthony, W. Hoyle and Yulong Ding, "Granular Materials Fundamentals and Applications", pp. 128, 2004.

21. Website: www.brycoat.com/tin/physprop.html, December 11, 2006.

22. James W. Robinson, "Undergraduate Instrumental Analysis", 2004.

23. Hugh O. Pierson, New Mexico, "Handbook of Chemical Vapor Deposition (CVD), Principles, Technology, and Applications", pp 98-105, 1992.

24. Hollahan .J.R. and Rosler .R.S, "Plasma Deposition of Inorganic Thin Films", in Thin Film Proces, Academic Press, New York, 1987.

25. Bachman P.K, Gartner G and Lydtin H, "Plasma-Assisted CVD Process", MRS Bulletin, pp. 51-59, Dec-1988.

26. Sherman A, "Chemical Vapor Deposition for Microelectronics", Noyes Publications, Park Ridge, NJ,1987.

27. K. K. Schuegraf, Ed. "Handbook of Thin Film Deposition Process and Techniques", Noyes Publications, Park Ridge, NJ, 1987.

28. Powell C.F, Oxley J.H and Blocher J.M, Jr., "Vapor Deposition", John Wiley and Sons, New York, 1966.

29. G. Lu, L. L. Tedder, and G. W. Rubloff, J. Vac. "Process Sensing and Metrology in Gate Oxide Growth by Rapid Thermal Chemical Vapor Deposition using SiH_4 and N_2O", Sci. Technol. vol.17 (4), pp. 1417-1423, Jul/Aug 1999.

30. Pieter Burggraaf, CVD Purity: "Gas and Tool Concerns". Semiconductor International, pp.70-75, March 1990.

31. Smoak B.C, Jr. and O'Ferrell D, "Gas Control Improves Epi Yield". Semiconductor International, pp. 88-92, June 1990.

32. Kearny K. "ECR Finds Applications in CVD". Semiconductor International, pp. 66-68, March 1989.

33. Bo-In Noh, Chang-Sung Seok, Won-Chul Moon and Seung-Boo Jung "Effect of Plasma Treatment on Adhesion Characteristics at Interfaces between Underfill and Substrate", International Journal of Adhesion and Adhesives, vol. 27, Issue 3, April 2007, pp. 200-206.

34. Website: http://en.wikipedia.org/wiki/Sputtering. November 23, 2006.

35. Website: http://www.mbe-components.com/products/ebeam/hv.html. December 18, 2007

36. Stuart F. Cogan, Philip R. Troyk, Julia Ehrlich, Timothy D. Plante, and David E. Detlefsen, "Potential-Biased, Asymmetric Waveforms for Charge-Injection with Activated Iridium Oxide (AIROF) Neural Stimulation Electrodes", IEEE transaction on Biomedical Engineering, vol. 53, No. 2, February 2006.

37. Stuart F. Cogan, Philip R. Troyk, Julia Ehrlich, and Timothy D. "In Vitro Comparison of the Charge-Injection Limits of Activated Iridium Oxide (AIROF) and Platinum-Iridium Microelectrodes", IEEE transaction on Biomedical Engineering, vol. 52, No. 9, September 2005.

38. Donaldson N. "When are Actively Balanced Biphasic Stimulating Pulses Necessary in a Neurological Prosthesis"? Medical and Biological Engineering and Computing, vol. 24, pp 50-56, January 1986.

39. Mortimer J.T., Kaufman D, and Roessman U, "Intramuscular Electrical Stimulation: Tissue Damage", Annals of Biomedical Engineering, vol. 8, pp. 235-244, 1980.

40. Huang C.Q, P. M. Carter, R. K. Shepherd. "Stimulus Induced pH Changes in Cochlear Implants: An In Vitro and In Vivo Study", Annals of Biomedical Engineering, vol. 29, pp.791-802, 2001.

41. Winfried Mayr, Manfred Bijak, Dietmar Rafolt, Stefan Sauermann, Ewald Unger, Hermann Lanmuller. "Basic Design and Construction of the Vienna FES Implants: Existing Solutions and Prospects for New Generations of Implants", Medical Engineering and Physics 23, pp. 53–60, 2001.

42. Amy P. Chu, Kjersti Morris, Robert J. Greenberg and David M. Zhou, "Stimulus Induced pH Changes in Retinal Implants", 26th Annual International Conference of the IEEE, vol.2, pp.4160-4162, 2004.

43. Christie Q. Huang, Robert K. Shepherd, Paul M. Carter, Peter M. Seligman, and Bruce Tabor, "Electrical Stimulation of the Auditory Nerve: Direct Current Measurement in Vivo", IEEE Transaction on Biomedical Engineering , vol.46, issue 4, pp.461-469, April 1999.

44. S. B. Brummer and M. J. Turner "Electrical Stimulation with Pt Electrodes: Estimation of Maximum Surface Redox (Theoretical Nongassing) Limits". IEEE Trans. Biomed. Eng., vol. BME-24, pp. 440-443, 1977.

45. L. S. Robblee, T. L. Rose, W. F. Agnew and D. B. Mc Creery, "Electrochemical Guidelines for Selection of Protocols and Electrode Materials for Neural Stimulation", in Neural Prostheses: Fundamental Studies, NJ: Prentice-Hall, pp. 25–66, 1990.

46. D.M. Zhou, R. J. Greenberg, "Electrochemical Characterization of Titanium Nitride Microelectrode Arrays for Charge-Injection Applications", Proceedings of the 25thAnnual International Conference of the IEEE EMBS, September 2003.

47. A. Hung, D. M. Zhou, R. I. Greenberg, and I. Judy, "Micromachined Electrodes for High Density Neural Stimulation System", 2nd Annual International, IEEE-EMS Special Topic Conference on Microtechnologies in Medicine & Biology, Madison, Wisconsin, pp.76-79, May 24, 2002.

48. A. Norlin, J.Pan and C. Leygraf, "Investigation of Electrochemical Behavior of Stimulating/Sensing Materials for Pacemaker Electrode Application", Journal of Electrochemical Society, pp. 152, July7, 2005.

49. Demetre J. Economou and Richard C. Alkire, "A Mathematical Model for a Parallel Plate Plasma Etching Reactor", Journal of Electrochemist Society, Solid-State Science and Technology, November 1998.